Article:
Huo, Y, Liu, T, Yang, Y et al. (3 more authors) (2020) In Situ Measurement of 3D Crystal Size Distribution by Double-View Image Analysis with Case Study on l-Glutamic Acid Crystallization. Industrial & Engineering Chemistry Research, 59 (10). pp. 4646-4658. ISSN 0888-5885

https://doi.org/10.1021/acs.iecr.9b05828

In-situ Measurement of 3D Crystal Size Distribution by Double-View Image Analysis with Case Study on L-glutamic Acid Crystallization

Journal:	*Industrial & Engineering Chemistry Research*
Manuscript ID	ie-2019-05828n
Manuscript Type:	Article
Date Submitted by the Author:	21-Oct-2019
Complete List of Authors:	Huo, Yan; Dalian University of Technology, Institute of Advanced Control Technology, School of Control Science & Engineering Liu, Tao; Dalian University of Technology, Institute of Advanced Control Technology, School of Control Science & Engineering Yang, Yixuan ; Dalian University of Technology, Institute of Advanced Control Technology, School of Control Science & Engineering Ma, Cai; Particle Science and Engineering, Wang, Xue Zhong; University of Leeds, School of Chemical and Process Engineering

In-situ Measurement of 3D Crystal Size Distribution by Double-View Image Analysis with Case Study on L-glutamic Acid Crystallization

Yan Huo [a,b,c], Tao Liu [a,b,*], Yixuan Yang [a,b], Cai Y. Ma [d], Xue Z. Wang [d, e]

[a]*Key Laboratory of Intelligent Control and Optimization for Industrial Equipment of Ministry of Education, Dalian 116024, China*

[b]*Institute of Advanced Control Technology, Dalian University of Technology, Dalian 116024, China*

[c]*College of Information Engineering, Shenyang University, Shenyang 110044, China*

[d]*Institute of Particle Science and Engineering, School of Chemical and Process Engineering, University of Leeds, Leeds LS2 9JT, UK*

[e]*School of Chemistry and Chemical Engineering, South China University of Technology, Guangzhou 510006, China*

** Corresponding author. Tel: +86-411-84706465; Fax: +86-411-84706706; E-mail: liurouter@ieee.org*

Abstract: In this paper, an in-situ measurement method is proposed for monitoring three-dimensional (3D) crystal size distribution (CSD) during a crystallization process, based on a binocular micro-vision system. The stereo particle shape is reconstructed from double-view images captured by two microscopic cameras fixed at different angles outside the crystallizer. To overcome the influence from solution turbulence and uneven illumination background involved with in-situ imaging, a microscopic double-view image analysis method is established to identify the key corners of each particle shape in the captured images, including corner detection and corner matching. Two fast algorithms are therefore given for on-line detection of two typical crystal morphologies of prismatic and needle-like shapes, such as α- and β-forms of L-glutamic acid (LGA) crystals, respectively. Based on the identified key corners for different particle shapes, a 3D geometry model is established to approximately reconstruct the 3D shape for each imaged particle, such that 3D sizes of each particle could be quantitatively estimated, along with the particle volume. Experiments on the LGA cooling crystallization are performed to demonstrate the effectiveness of the proposed method.

Keywords: Crystal size distribution, three-dimensional (3D) particle size measurement, binocular micro-vision system, 3D geometry reconstruction, corner detection, L-glutamic acid crystallization.

1. Introduction

The crystallization technology has been widely used for separating different components from solution and purifying particle products in chemical and pharmaceutical industries. For control and optimization of crystallization processes, on-line process analytical technologies (PATs) have been explored for assessing the crystal morphology, growth rate and quality [1-4]. With a rapid development of the photoelectric technology, on-line image based monitoring methods were increasingly studied for measuring the sizes and shape of crystals [5-9]. Based on image analysis of multi-dimensional crystal sizes and shape feature, a few crystal morphology analysis methods were developed for monitoring the crystal quality during crystallization [10, 11]. The developed imaging systems for monitoring crystallization processes mainly include two types: invasive and non-invasive. For using an invasive imaging system, e.g., the digital particle vision and measurement (PVM) [12] , the imaging probe could be stuck into the crystal slurry to capture the crystal images. A novel invasive imaging probe was recently developed based on the existing image analysis methods to cope with blurry images with noise [13]. In contrast, a non-invasive imaging system is installed outside a crystallizer to image the crystallization process by the observation window [14, 15]. Compared with an invasive imaging system, a non-invasive imaging system could avoid the contamination of camera lens from the crystal slurry. However, the lighting source of a non-invasive imaging system needs to be carefully installed in an opposite position to the cameras outside the crystallizer, in order to provide sufficient illumination for real-time imaging.

With crystal images captured by an invasive or non-invasive imaging system, Larsen et al. [16] developed an efficient image processing algorithm for analyzing the crystal size distribution (CSD) of high-aspect-ratio crystals. Zhang et al. [17] proposed a few particle shape descriptors based on the principal component analysis (PCA) to classify polymorphic organic crystals during batch crystallization. A synthetic image analysis method [11] was recently presented for in-situ crystal size measurement and shape identification. Gao et al. [8] proposed an in-situ measurement method based on the recently developed deep learning technology to classify α- and β-forms of L-glutamic acid (LGA) crystals and measure the two-dimensional (2D) sizes of length and width, along with an estimation of the surface area. This approach needs a large amount of samples of α- or β-form

crystals for off-line training along with a demanding computation effort. For monitoring the crystal growth quality, it was pointed out that 2D image analysis methods could provide relatively less information than those of 3D imaging methods [18-20]. Bujak and Bottlinger [21] adopted three orthogonally installed cameras to measure 3D sizes of particles with irregular shapes, but not for imaging crystals in the slurry. An off-line 3D shape measurement method was developed based on assembling the 2D surface images of a crystal captured by using a regular reflection of light [22]. Another off-line 3D size measurement method [23] was proposed for cuboid crystals such as β-form LGA, by using a multi-projection imaging system consisting of one camera and two mirrors. This approach was subsequently extended for on-line measurement by imaging a flow through cell using a sampling loop with two external cameras installed orthogonal to each other [24], which was mainly devoted to cuboid crystals. Borchert et al. [25] developed an alternative image analysis method for reconstructing the 3D crystal shape from the corresponding 2D crystal projections, where the Fourier descriptors were used to detect the crystal shape outline based on a pre-defined database of different crystal shapes. Recently, a new dual-camera measurement device was developed for real-time monitoring of particle shapes rather than 3D size measurement via a circulating pipeline [26], based on an image segmentation algorithm for background extraction and a volume intersection method for classification of different 3D particle shapes. Ma et al. [27] presented a proof-of-concept of 3D shape reconstruction based on using two no-invasive cameras installed with a pre-specified angle to synchronously capture images, which was further extended in the references [20, 28] for roughly estimating 3D size growth of crystals rather than quantitative measurement. For using a binocular micro-vision system to capture stereo images for analysis, a few calibration methods for guaranteeing the measurement accuracy were reported in the references [29, 30], but these methods could not be used for in-situ installed micro-vision systems subject to uneven illumination background, particle motion, and solution turbulence usually involved with crystallization processes. Although the recent work [31] developed a microscopic double-view image analysis method for in-situ measurement of 2D particle sizes, it remains open to measure the third dimensional particle size that could be perpendicular to the 2D imaging plane, and therefore, the particle volume could not be estimated therein.

To tackle the difficulty of measuring 3D sizes and volumes of particles during crystallization, an in-situ image-based measurement method is proposed in this paper with application to the cooling crystallization processes of α- and β-form LGA crystals, based on a non-invasive binocular micro-vision system. Firstly, two fast image analysis algorithms are given for identifying the key corners of two typical crystal morphologies, i.e., prismatic α-form and needle-like β-form of LGA crystals, respectively. Then, a binocular geometric model is constructed for computing the 3D space location of each corner. Based on the computed 3D coordinates of these key corners, a 3D geometry model is established to approximately reconstruct the 3D particle shape, which is therefore used for measuring the 3D sizes of each particle in the in-situ captured images. A measurement test on a micro-scale ruler placed in 3D location is conducted to verify the accuracy of the proposed method for 3D size measurement. In addition, another fast algorithm is given for computing the volumes of particles with image reconstruction, for the convenience of real-time application. Experiments on monitoring the cooling crystallization process of LGA are performed to demonstrate the effectiveness of the proposed method for in-situ measurement of particle sizes.

2. Experimental set-up

2.1 Non-invasive binocular micro-vision system for in-situ measurement

The experimental set-up for using a non-invasive binocular vision system to monitor a cooling crystallization process is shown in Fig.1, where the crystallizer consists of a 4L jacketed glass reactor (ACE-AIO 4000), a 4-paddle agitator (PTFE), a thermostatic circulator (Julabo-CF41), and a temperature probe (Pt100). The non-invasive binocular vision system for in-situ imaging during crystallization was made by Hainan Six Sigma Intelligent Systems Ltd. (product no. Stereo Vision Crystal-G), which consists of two microscopic cameras and two lighting sources commanded by a light controller (Gardasoft RT260-20) for snapshot. Each camera has a CCD sensor with the maximum pixel resolution of 2448×2048 and a micro lens set at a distance of 40mm from the reactor glass wall (the maximum working distance is about 65mm). The maximum frame rate is 6.5 fps for each camera. For in-situ measurement, two microscopic cameras are situated up and down in a line outside the glass vessel so as to alleviate the distortion for capturing images, while

there is an intersection angle of 12.5 degree between the optical axes of two cameras. The lighting sources are installed in line with the camera lens on the other side of the glass vessel, providing the lighting illumination of 350lux. For real-time analysis, a pair of microscopic images is synchronously shot via two cameras per two seconds during the crystallization process.

2.2 Crystallization material of LGA

The solute material used in this study is LGA ($C_5H_9NO_4$). LGA has two typical polymorphic forms [5, 32], prismatic α-form and needle-like β-form, as shown in Fig.2. Different linear cooling rates [5] were studied to procure these two product forms. In this work, the LGA solution was taken as distilled water.

To perform a cooling crystallization experiment of LGA, the solution is initially heated up to 70°C and then maintained at the temperature until all the LGA solute is completely dissolved. After that, the solution is cooled down to 20°C by a specified cooling rate and maintained at the temperature until the end of experiment. The agitator is operated at a constant rate of 200 rpm to maintain the uniformity of particle distribution in the suspension during crystallization.

3. Double-view image analysis on the key corners of particle shapes

Since double-view images in-situ captured by a non-invasive binocular vision system shown in Fig.1 were blurred by solution turbulence and uneven illumination background, it is necessary to identify salient features of particle shapes in these images for analyzing 3D particle morphology and sizes. To exclude the noise affect, the well-known median filter [33] may be used to recover the denoised grayscale images from the captured images for real-time analysis. Then, a multi-scale segmentation with the Canny operator [34] is preferred to detect the particle shape edge from a denoised image. Note that any unobvious edge points could be removed by using a specified threshold. By filling the gaps between identified edge points with their adjacent edge features, the contour edge of each particle image could be determined in an efficient manner.

For reconstructing 3D particle shapes based on the pre-processed images to measure the particle 3D sizes, it is proposed to detect the key corners of each particle. LGA crystals have two typical polymorphic forms, prismatic α-form and needle-like β-form [8, 35], as shown in Fig.2a. Note

that these two shapes could be distinguished from in-situ captured images by using the inner distance descriptor introduced in the previous work [11]. However, their key corners are distinct from each other in the geometric location for shape reconstruction, as shown in Fig.2b. Concerning an α-form crystal, the 3D image contour after edge detection includes external and internal edges, and correspondingly, there are eight key corners to be detected, including four external and internal key corners, respectively. In contrast, a β-form crystal has a needle-like shape where the key corners are located at both ends of the image contour. Two different algorithms are therefore proposed to detect the key corners of α- and β-form crystals, respectively.

For detecting the key corners of an α-form crystal, the coordinates of all the contour points are denoted by (x_n, y_n), where $n = 1, 2, \mathsf{K}, N$, and therefore, the centroid coordinate denoted by (x_c, y_c) is defined by

$$\begin{cases} x_c = \dfrac{1}{N}\sum_{n=0}^{N-1} x_n \\ y_c = \dfrac{1}{N}\sum_{n=0}^{N-1} y_n \end{cases} \tag{2}$$

Correspondingly, the inner distances from the centroid to the boundary points are defined by

$$d_n = \sqrt{(x_c - x_n)^2 + (y_c - y_n)^2} \tag{3}$$

The inner distances of all the contour points are plotted in Fig.3, where the peak points are defined as the extremum points of the contour. The set of each edge point is composed of the boundary points between every two edge extreme points. The fitting lines $y = a_j x + b_j, \quad j = 1, \ldots, 4$ along each edge are optimized by a least-squares (LS) algorithm as

$$\begin{cases} a_j = \dfrac{1}{C^j}\sum_{k=1}^{K} (x_k{}^j - \overline{x}^j)(y_k{}^j - \overline{y}^j) \\ b_j = \overline{y}^j - a_j \overline{x}^j \end{cases} \tag{4}$$

where $C^j = \sum_{k=1}^{K} (x_k{}^j - \overline{x}^j)^2$, and K is the point number.

The key corners of either external or internal contour edges are determined by computing the crossover points of the above fitting lines. Note that the external and internal key corners are detected for determining the external and internal contour edges, respectively, as shown in Fig.2b.

For clarity, the proposed corner detection algorithm for prismatic α-form crystals is

summarized below.

Step 1: Find the external or internal contour edges using the Canny edge detector;

Step 2: Define the extremum points of external or internal contour edges in a particle image, by computing the centroid coordinates of the external or internal contour edges via Eq.(2) and the inner distances of all the contour points via Eq.(3), and then choosing the peak points in the plot of the inner distances;

Step 3: Fit the external contour edges in a particle image by optimizing the fitting lines along each edge via Eq.(4);

Step 4: Determine the external and internal key corners by computing the crossover points of the above fitting lines.

For detecting the key corners of a β-form crystal, the candidate corners are selected based on the curvature scale-space method that has good robustness against noise [36, 37]. For the particle contour described by $\psi(u) = \left(x(u), y(u)\right)$, where u denotes the length parameter, the corresponding multi-scale curve $\psi(u,\sigma)$ under a scale σ is defined by

$$\psi(u,\sigma) = \left(X(u,\sigma), Y(u,\sigma)\right) \tag{5}$$

where

$$\begin{cases} X(u,\sigma) = x(u) * g(u,\sigma) \\ Y(u,\sigma) = y(u) * g(u,\sigma) \end{cases} \tag{6}$$

where $*$ denotes the convolution operator, and $g(u,\sigma)$ denotes a Gaussian function with the standard deviation σ.

The curvature of $\psi(u,\sigma)$ is computed by

$$\psi(u,\sigma) = \frac{X_u(u,\sigma)Y_{uu}(u,\sigma) - X_{uu}(u,\sigma)Y_u(u,\sigma)}{\left(X(u,\sigma)^2 + Y(u,\sigma)^2\right)^{1.5}} \tag{7}$$

where $X_u(u,\sigma)$ and $X_{uu}(u,\sigma)$ are the first and second order derivatives of $X(u,\sigma)$ with respect to u. $Y_u(u,\sigma)$ and $Y_{uu}(u,\sigma)$ are the first and second order derivatives of $Y(u,\sigma)$ with respect to u.

According to Eq.(7), the curvature $\psi(u,\sigma_j)$ of an edge point on the scale j can be

computed, and then the curvature product at four different scales is computed as

$$\Gamma(u) = \prod_{j=1}^{4} \psi(u, \sigma_j) \tag{8}$$

Subsequently, a local maximum edge point with a curvature product greater than a specified threshold, e.g., $T = 0.03$ given in the reference [37] for corner detection, is taken as a candidate corner. Considering that corner points should be at both ends of the crystal shape as shown in Fig.2b, the key corners are determined by specifying a criterion, i.e., the inner distance of a candidate corner should be no less than one third of the crystal length.

Hence, the proposed corner detection algorithm for need-like β-form crystals is summarized below.

Step 1: Find the external contour edges using the Canny edge detector;

Step 2: Define the corners of the contour edges in a particle image by the curvature scale-space approach using Eqs.(4-7);

Step 3: Exclude those corners not complying with the inner distance criterion.

After the key corner detection, matching the key corners between double-view images is conducted by using the BRIEF descriptor [38] owing to its robustness and fast speed for real-time application. To determine the descriptor, a square region I of size $S \times S$ (i.e., pixel number) is chosen around such a key corner. Denote by p_i and q_i two different pixel points located in I, where i is the pixel index and N is 256. To avoid sensitivity to noise, each region is preprocessed by the Gaussian smoothing approach [38]. Then, an N-bit vector denoting the BRIEF descriptor is defined by

$$b_N(I) = \sum_{1 \le i \le N} 2^{i-1} g(I; p_i, q_i) \tag{9}$$

where

$$g(I; p_i, q_i) = \begin{cases} 1 & if\ I(p_i) < I(q_i) \\ 0 & \text{otherwise} \end{cases} \tag{10}$$

where $I(p_i)$ and $I(q_i)$ are the intensities of p_i and q_i in the region I. Note that (p_i, q_i) follow the Gaussian distribution of $(0, 1/25S^2)$.

The similarity between corner descriptors computed from double-view images is then measured by the Hamming distance [38], which determines the matching pairs of key corners in double-view images in terms of the maximum similarity degree.

It should be noted that the quality of particle morphology reconstruction depends on the identified key corners, which is affected by 3D location of each particle in the captured images.

4. Stereo shape reconstruction and measurement of 3D particle sizes

Based on the identified key corners in double-view images, a 3D geometry model is proposed to approximately reconstruct the stereo shape of each particle appearing in double-view images. Correspondingly, the 3D sizes and volume of each particle are measured based on the established 3D geometry model. An error analysis is given to verify the accuracy of the proposed method, along with an experiment on measuring a micro-scale ruler by using the non-invasive binocular micro-vision system shown in Fig.1.

4.1 3D geometry model

Fig.4a shows a geometry model case of imaging a space point denoted by P with the non-invasive binocular micro-vision system shown in Fig.1, where the left-view and right-view images are captured from the installed upper and lower cameras, respectively. The model origin of the 3D coordinate system is set to the left-view centroid as shown in Fig.4a, denoted by O. For 3D shape reconstruction, the 3D coordinate (X,Y,Z) of a space point P is a function of the 2D coordinates denoted by P_l and P_r in the double-view projections. Denote by $P_l(u_l,v_l)$ and $P_r(u_r,v_r)$ the imaging points from the left-view and right-view, respectively, both of which have the same size of $L\times H$ (length × height) with P. Denote by γ the pixel equivalent without amplification, by κ the amplification coefficient, by b the baseline length, and by 2θ, $(0<\theta<90^{\circ})$ the stereo angle.

Without loss of generality, the 3D coordinate (X,Y,Z) of P is derived as

$$\begin{cases} X = Z\tan(\theta + p\tau_l) \\ Y = \gamma(v_l - H/2) \\ Z = bf\cos\theta/(2f\sin\theta + a_l + a_r) \end{cases} \tag{11}$$

Correspondingly, the key parameters of a_l and a_r in Eq.(11) that depend on the locations of point projection (i.e. u_l and u_r) in these images are derived as

$$a_l = p\frac{x_l \cos\tau_l}{\cos(\tau_l + p\theta)} \tag{12}$$

$$a_r = q\frac{x_r \cos\tau_r}{\cos(\tau_r + q\theta)} \tag{13}$$

with

$$p = \begin{cases} 1, & u_l \geq L/2 \\ -1, & u_l < L/2 \end{cases} \tag{14}$$

$$q = \begin{cases} -1, & u_r \geq L/2 \\ 1, & u_r < L/2 \end{cases} \tag{15}$$

where $\tan\tau_l = x_l / f$, $x_l = \frac{\gamma}{\kappa}|u_l - L/2|$, $\tan\tau_r = x_r / f$, $x_r = \frac{\gamma}{\kappa}|u_r - L/2|$.

For comprehension, a brief derivation of Eq.(11) for the case of $u_l \geq L/2$ and $u_r \geq L/2$ as shown in Fig.4a, is given in the Appendix. Similarly, the computational formulae of the 3D coordinate (X,Y,Z) of a space point P can be derived for the other three cases, $u_l \geq L/2$ and $u_r < L/2$; $u_l < L/2$ and $u_r \geq L/2$; $u_l < L/2$ and $u_r < L/2$, which are omitted for brevity.

Hence, the 3D coordinates of all the key corners in the image contour of each particle can be computed, and therefore, are used to approximately reconstruct the 3D geometry model of each particle shape, as shown in Fig.2.

4.2 Measurement error analysis

The derivation in the above section indicates that the 3D coordinates of key corners depend on the structural parameters of the non-invasive binocular micro-vision system shown in Fig.1, i.e., the pixel equivalent and the location of the image points. The 3D coordinate of such a space point can be expressed as a vector function,

$$(X,Y,Z) = F(f,b,\theta,\gamma,u_l,u_r) \tag{16}$$

It is therefore seen that the measurement error arises from the structural parameter error ($\Delta f, \Delta b, \Delta\theta$), the size calibration error $\Delta\gamma$, and the image corner extraction error ($\Delta u_l, \Delta u_r$). In fact, the structural parameter error could be negligible or reduced to a very small value if the non-invasive binocular micro-vision system is properly installed. Therefore, the size calibration error

and image corner extraction error should be mainly considered to ensure the 3D measurement accuracy. It should be noted that the size calibration error is affected by the imaging object distance. Hence, different pixel equivalent values should be taken into account with respect to different imaging object distances, especially for a large depth-of-field imaging system.

Verification of the measurement error is necessary for practical application. However, few references addressed feasible verification methods for micro-scale particle size measurement. It remains open as yet to verify the accuracy and reliability of measuring 2D or 3D particle sizes by using a micro-vision system. To tackle the difficulty, two critical indices including the space size and dip angle are therefore introduced for assessing accuracy of the reconstructed stereo shape for an imaged particle. Note that the dip angle is a 3D index which is not needed for 2D measurement. In this study, a linear micro-scale ruler is used for experimental verification, in consideration of that different sizes can be directly exemplified in micro-scale. Meanwhile, a geometric holder is used to provide a dip angle of 65^{o} for placing the micro-scale ruler to conduct 3D measurement. Fig.5 shows a schematic diagram of the experimental verification. The measurement results for the line segments from point B to point C (denoted by B-C), from point A to point C (denoted by A-C) and from point A to point D (denoted by A-D) are listed in Table 1, where the relative measurement error is defined by

$$E = |a - b| / b \times 100\% \tag{17}$$

where a is the measured value, and b is the true value.

It is seen that the averaged relative error for measuring these segments is smaller than 5%, while the averaged relative error for measuring the dip angle is only about 5%, well demonstrating good accuracy of the proposed 3D measurement method. Note that if the structural parameters of the imaging system could be measured more precisely, the relative error will be further reduced.

4.3 Measurement of 3D sizes and particle volume

The reconstructed 3D geometry model for each particle is used to measure the 3D sizes (namely, length, width and height) and particle volume. In view of that the 3D shapes for α- and β-form particles are obviously different from each other, as shown in Fig.2, the corresponding measurement algorithms are proposed below, respectively.

For an α-form particle, it is seen from Fig.2b that there are four external and internal key corners, respectively. Denote the external corner points by $\{P_{\mathrm{e}}^{n}(x_{\mathrm{e}}^{n}, y_{\mathrm{e}}^{n}, z_{\mathrm{e}}^{n}), n=1,2,3,4\}$ and the internal corner points by $\{P_{\mathrm{i}}^{n}(x_{\mathrm{i}}^{n}, y_{\mathrm{i}}^{n}, z_{\mathrm{i}}^{n}),\ n=1,2,3,4\}$. To describe the length of the reconstructed 3D geometry model, the length of α-form particle is computed as

$$S_{\mathrm{l}} = \max(d_{\mathrm{l}}^{n}),\ \ n=1,2,3,4 \tag{18}$$

where d_{l}^{n}, $n=1,2,3,4$ denote the line segment lengths $D(P_{\mathrm{e}}^{1}, P_{\mathrm{e}}^{2})$, $D(P_{\mathrm{e}}^{2}, P_{\mathrm{e}}^{3})$, $D(P_{\mathrm{e}}^{3}, P_{\mathrm{e}}^{4})$ and $D(P_{\mathrm{e}}^{4}, P_{\mathrm{e}}^{1})$, respectively.

Correspondingly, the width of α-form particle is computed as

$$S_{\mathrm{w}} = \min(d_{\mathrm{w}}{}^{n}),\ \ n=1,2,3,4 \tag{19}$$

where $d_{\mathrm{w}}{}^{n}$, $n=1,2,3,4$ denotes the distances between P_{e}^{1} and the line segment $P_{\mathrm{e}}^{3}P_{\mathrm{e}}^{4}$, P_{e}^{2} and the line segment $P_{\mathrm{e}}^{1}P_{\mathrm{e}}^{4}$, P_{e}^{3} and the line segment $P_{\mathrm{e}}^{1}P_{\mathrm{e}}^{2}$, P_{e}^{4} and the line segment $P_{\mathrm{e}}^{2}P_{\mathrm{e}}^{3}$, respectively.

To compute the height of the reconstructed 3D geometry model, two fitting planes of the external and internal corner points are constructed, respectively. Suppose a fitting plane expressed by $ax+by+cz=d$, where a, b, c are unit normal vectors of the plane, satisfying $a^2+b^2+c^2=1$ and $d\geq 0$. For four space points denoted by $\{P_n(x_n, y_n, z_n), n=1,2,3,4\}$, a recognized optimization program [39] for determining the fitting plane parameters (a,b,c,d) can be used,

$$\min_{a,b,c,d} \sum_{n=1}^{4} (ax_n + bx_n + cz_n - d)^2 \tag{20}$$

To solve the above optimal program, let $s_n = | ax_n + by_n + cz_n - d |$ and a penalty function with the Lagrange multiplier is defined by

$$f = \sum_{n=1}^{4} s_n{}^2 - \lambda(a^2+b^2+c^2-1) \tag{21}$$

The derivative of Eq.(21) with respect to d is obtained as

$$\frac{\partial f}{\partial d} = -2\sum_{n=1}^{4} (ax_n + bx_n + cz_n - d) \tag{22}$$

By letting (22) be zero, it yields

$$d = a\frac{\sum_{n=1}^{4} x_n}{4} + b\frac{\sum_{n=1}^{4} y_n}{4} + c\frac{\sum_{n=1}^{4} z_n}{4} \tag{23}$$

Similarly, by letting the derivative of Eq. (21) with respect to a, b, c be zero, respectively, there follows

$$\begin{cases} \sum_{n=1}^{4}(a\Delta x_n + b\Delta x_n + c\Delta z_n)\Delta x_n - \lambda a = 0 \\ \sum_{n=1}^{4}(a\Delta x_n + b\Delta x_n + c\Delta z_n)\Delta y_n - \lambda b = 0 \\ \sum_{n=1}^{4}(a\Delta x_n + b\Delta x_n + c\Delta z_n)\Delta z_n - \lambda c = 0 \end{cases} \tag{24}$$

where $\Delta x_n = x_n - \overline{x}_n$, $\Delta y_n = y_n - \overline{y}_n$, and $\Delta z_n = z_n - \overline{z}_n$.

The eigenvalue equation of Eq.(24) is defined by

$$\boldsymbol{A}\boldsymbol{x} = \lambda \boldsymbol{x} \tag{25}$$

where

$$\boldsymbol{x} = (a, b, c)^T \tag{26}$$

$$\boldsymbol{A} = \begin{bmatrix} \Delta x_n \Delta x_n & \Delta x_n \Delta y_n & \Delta x_n \Delta z_n \\ \Delta x_n \Delta y_n & \Delta y_n \Delta y_n & \Delta y_n \Delta z_n \\ \Delta x_n \Delta z_n & \Delta y_n \Delta z_n & \Delta z_n \Delta z_n \end{bmatrix} \tag{27}$$

The eigenvalue value of Eq.(25) can be solved as

$$\lambda = \frac{(\boldsymbol{A}\boldsymbol{x}, \boldsymbol{x})}{(\boldsymbol{x}, \boldsymbol{x})} = \sum_{n=1}^{4}(a\Delta x_n + b\Delta x_n + c\Delta z_n)^2 = \sum_{n=1}^{4} {s_n}^2 \tag{28}$$

where $(,)$ denotes the inner product of two vectors.

The minimum of $\sum_{n=1}^{4} {s_n}^2$ corresponds to the smallest eigenvalue of $\boldsymbol{A}$, which therefore determines the optimal eigenvector (a, b, c). Hence, the optimal fitting planes of the external and internal corner points could be determined, respectively.

Considering that the fitting plane of the external corner points may not be in parallel with that of the internal corner points, the height of an α-form particle is computed as

$$S_{\mathrm{h}} = \frac{1}{4}\sum_{n=1}^{8} {d_{\mathrm{h}}}^n \tag{29}$$

where ${d_{\mathrm{h}}}^n$, $n = 1, 2, \mathrm{L}, 8$ denotes the distances between the point P_{e}^n and the fitting plane of $(P_{\mathrm{i}}^1, P_{\mathrm{i}}^2, P_{\mathrm{i}}^3, P_{\mathrm{i}}^4)$, the point P_{i}^n and the fitting plane $(P_{\mathrm{e}}^1, P_{\mathrm{e}}^2, P_{\mathrm{e}}^3, P_{\mathrm{e}}^4)$, respectively. Note that owing to the α-form particle is symmetrical with respect to the fitting plane composed of the external corner points, the height is computed as double of the averaged distance between these two fitting planes.

For a β-form particle, the identified key corners are used to reconstruct a 3D geometry model of the cuboid shape. Owing to that the cuboid shape could be efficiently approximated by the minimum-volume bounding box approach [40, 41], 3D sizes of a β-form particle can therefore be measured by using this approach for the reconstructed cuboid.

Based on the above measured 3D sizes, the particle volume can be quantitatively computed, such as from a reconstructed cuboid. However, such computation may give rise to undesirable estimation error. To improve the computation accuracy, it is proposed to view the reconstructed particle shape as a convex hull for computation. By using the Delaunay triangulation principle [42], a convex hull can be subdivided into N_s tetrahedrons. Denote by $\{(x_{t,n}, y_{t,n}, z_{t,n}), t = 1,...,4, n = 1,...,N_s\}$ four vertex coordinates of the n-th tetrahedron, the volume of the n-th tetrahedron can be computed as

$$V_n = \frac{1}{6} \times \begin{vmatrix} 1 & 1 & 1 & 1 \\ x_{1,n} & x_{2,n} & x_{3,n} & x_{4,n} \\ y_{1,n} & y_{2,n} & y_{3,n} & y_{4,n} \\ z_{1,n} & z_{2,n} & z_{3,n} & z_{4,n} \end{vmatrix} \tag{30}$$

Accordingly, the particle volume is estimated based on the symmetry as

$$V = 2\sum_{n=1}^{N_s} V_n \tag{31}$$

5. Experimental results

Two cooling crystallization experiments on α- and β-form LGA were performed, respectively, based on the non-invasive binocular imaging system for 3D morphology measurement, with the same experimental conditions introduced in Section 2, except for the cooling rates of 1°C/min for α-form LGA and 0.2°C/min for β-form LGA. Note that to transform the image pixel into a physical unit for computation, the calibration method [11] with circle scale was used to obtain the pixel equivalent before the measurement. For comparison, an off-line electron microscope (Leica DM 2500, LAS_v4.4) was also used for verifying the sizes and volumes of final crystal products.

Before 3D reconstruction of particle shapes, image processing was conducted for in-situ captured double-view images of α-form LGA crystals during the crystallization process, as shown

in Fig.6. For illustration, a pair of the original double-view images including α-form crystals is shown in Fig.6a. Fig.6b shows the preprocessed image pair of the outlined α-form crystal in Fig.6a by the Canny method. Using the proposed corner detection method for α-form crystals, Fig.6c shows the detected results of external and internal contour edges of this α-form crystal. Accordingly, the corner detection results are shown in Fig.6d, well demonstrating that the proposed image analysis method effectively detected the key corners in real time. The detected key corners were then used for 3D reconstruction of this crystal shape.

A reconstructed stereo shape of α-form crystals is illustrated in Fig.7. The 3D coordinates of the eight key corners are computed by the proposed geometry model formulae, as shown in Fig.7a. The correspondingly reconstructed 3D geometry model is shown in Fig.7b. Note that the symmetry of an α-form crystal should be considered in the final geometry reconstruction, which is omitted.

Similarly, a stereo reconstruction of β-form LGA crystals is illustrated in Fig.8, based on the in-situ captured double-view images. Fig.8a shows the in-situ captured images of β-form crystals. After image preprocessing, the segmented double-view images for a sampled β-form crystal are shown in Fig.8b. Then Fig.8c shows the corner detection results for this β-form crystal. Finally, a stereo shape of this β-form crystal is approximately reconstructed based on the corresponding key corners, as shown in Fig.8d.

Note that the total time spent for the proposed method to measure the 3D sizes of an α- form LGA crystal was about 1.52 seconds, and about 1.48 seconds for a β-form LGA crystal, based on a monitoring computer configured with CPU of Intel 3.40 GHZ and RAM of 8.00G. The time was sufficiently small for implementing an on-line control strategy as studied in the recent paper [43], where the sampling time for control implementation was taken as tens of second or even a few minutes for LGA cooling crystallization.

To demonstrate the effectiveness of the proposed method, an off-line measurement of CSD using an electron microscope was also performed on the final crystal products for verification. In view of that an electron microscope could only measure the 2D sizes of each crystal, comparison between the proposed method and an electron microscope was therefore made for measuring the CSDs in length and width for LGA crystal products of α-and β-forms, respectively. Almost 200

particles randomly taken from the LGA crystal products were used for measuring CSD of α- and β-form crystals, respectively. For illustration, the measured CSDs were fitted by the probability density estimation with the normal kernel function [44]. The measured CSD results are plotted in Fig.9 in comparison with off-line measurement by an electron microscope based on the pre-processed samples of LGA crystal products, well demonstrating the consistency between each other.

To further demonstrate the superiority of the proposed method over the recently developed 2D size measurement method [11] based on the image projection of a particle in a 2D fitting plane, Table 2 shows a comparison of relative errors between the proposed method (denoted by 3DM) and the 2D size measurement method (denoted by 2DM) with reference to the off-line measurement by an electron microscope, where the peak size denotes the peak value of CSD. It is seen that evidently improved accuracy on the 2D size measurement is obtained by the proposed method.

In view of that the above LGA crystal products are too tiny in volume to be measured by an electron microscope for off-line verification, the needle-like monosodium glutamate crystals with relatively larger 3D sizes of millimeter-scale were used to verify the proposed volume computation method, owing to that their shapes are similar to β-form LGA crystals and these particles can be manually deployed for in-situ or off-line measurement. The experiment was carried out by fixing thee needle-like monosodium glutamate crystals on the inside wall of the glass crystallizer for in-situ measurement by the non-invasive binocular imaging system, as shown in Fig.10(a). The proposed volume computation method is therefore used based on 3D shape reconstruction. For comparison, the off-line measurement was conducted by measuring two side faces (length×width and length×height) of each particle with an off-line electron microscope for computing the particle volume, as shown in Fig.10(b). The measurement results are listed in Table 3. It is seen that the in-situ measurement results by the proposed method are in good agreement with the off-line measurement by an electron microscope, with averaged relative errors below 10%. These results well demonstrates that the proposed method can be effectively used for in-situ assessment of particle volumes during the crystallization process, thus facilitating on-line monitoring of crystal growth kinetics and quality.

6. Conclusions

An in-situ measurement method has been proposed for monitoring 3D CSD during a crystallization process, based on double-view images simultaneously captured by a non-invasive binocular micro-vision system. By detecting the particle edges from the captured double-view images with fast image preprocessing algorithms to overcome the influence from solution turbulence and uneven illumination background involved with in-situ imaging, two fast algorithms for real-time implementation are proposed to locate the key corners in the captured images for two typical crystal morphologies of prismatic and needle-like shapes, such as α- and β-forms of LGA, respectively. Based on the identified key corners, a 3D geometry model is established to approximate the 3D shape of each captured particle. Two fast algorithms are given to compute 3D sizes of α- and β-form LGA crystals from the reconstructed 3D shapes, respectively. In addition, a tetrahedron based fast algorithm is given to quantitatively measure the volume of each imaged particle. Experimental tests on the cooling crystallization processes of α- and β-form LGA crystals have well demonstrated the effectiveness of the proposed method for in-situ monitoring 3D crystal morphologies, with good accuracy on measuring the length and width of crystals in comparison with off-line measurement by an electron microscope or the recent 2D crystal size measurement method given in the previous work [11]. Moreover, the in-situ measurement accuracy on particle volume by the proposed method is validated via needle-like monosodium glutamate crystals, in comparison with off-line measurement by an electron microscope. It should be noted that the accuracy of such a 3D geometry model for approximation depends on the identified key corners. If no sufficient key corners could be detected for a particle image, its 3D morphology may not be completely reconstructed, in particular for very small particles that could not be effectively imaged. It therefore deserves a further study on multi-directional imaging with more cameras or a predefined data set to facilitate 3D shape reconstruction in the future work, along with real-time classification methods on different particle shapes.

Acknowledgements

This work was supported in part by the NSF China Grant 61633006, the Fundamental Research Funds for the Central Universities of China (DUT18ZD201), and National Key RD Program of China under Grant 2017YFA0700300.

References

(1) Yu, Z.; Chew, J.; Chow, P.; Tan, R., Recent advances in crystallization control: an industrial perspective. *Chemical Engineering Research and Design* **2007,** 85, (7), 893-905.
(2) Wang, X. Z.; Roberts, K. J.; Ma, C., Crystal growth measurement using 2D and 3D imaging and the perspectives for shape control. *Chemical Engineering Science* **2008,** 63, (5), 1173-1184.
(3) Nagy, Z. K.; Fevotte, G.; Kramer, H.; Simon, L. L., Recent advances in the monitoring, modelling and control of crystallization systems. *Chemical Engineering Research and Design* **2013,** 91, (10), 1903-1922.
(4) Borsos, A. k.; Szilagyi, B.; Agachi, P. S. e.; Nagy, Z. K., Real-time image processing based online feedback control system for cooling batch crystallization. *Organic Process Research & Development* **2017,** 21, 511-519.
(5) Anda, J. C. D.; Wang, X. Z.; Lai, X.; Roberts, K. J.; Jennings, K. H.; Wilkinson, M. J.; Watson, D.; Roberts, D., Real-time product morphology monitoring in crystallization using imaging technique. *AIChE Journal* **2005,** 51, (5), 1406-1414.
(6) Ferreira, A.; Faria, N.; Rocha, F.; Teixeira, J., Using an online image analysis technique to characterize sucrose crystal morphology during a crystallization run. *Industrial & Engineering Chemistry Research* **2011,** 50, (11), 6990-7002.
(7) Hansen, T. B.; Simone, E.; Nagy, Z.; Qu, H., Process analytical tools to control polymorphism and particle size in batch crystallization processes. *Organic Process Research & Development* **2017,** 21, 855-865.
(8) Gao, Z.; Wu, Y.; Bao, Y.; Gong, J.; Wang, J.; Rohani, S., Image analysis for in-line measurement of multidimensional size, shape, and polymorphic transformation of L-glutamic acid using deep learning-based image segmentation and classification. *Crystal Growth & Design* **2018,** 18, (8), 4275-4281.
(9) Eisenschmidt, H.; Voigt, A.; Sundmacher, K., Face-Specific growth and dissolution kinetics of potassium dihydrogen phosphate crystals from batch crystallization experiments. *Crystal Growth & Design* **2015,** 15, (1), 219-227.
(10) Liao, C. W.; Yu, J. H.; Tarng, Y. S., On-line full scan inspection of particle size and shape using digital image processing. *Particuology* **2010,** 08, (3), 286-292.
(11) Huo, Y.; Liu, T.; Liu, H.; Ma, C. Y.; Wang, X. Z., In-situ crystal morphology identification using imaging analysis with application to the L-glutamic acid crystallization. *Chemical Engineering Science* **2016,** 148, 126-139.
(12) Zhou, Y.; Srinivasan, R.; Lakshminarayanan, S., Critical evaluation of image processing approaches for real-time crystal size measurements. *Computers & Chemical Engineering* **2009,** 33, (5), 1022-1035.
(13) Arnaout, T. E.; Cullen, P. J.; Sullivan, C., A novel backlight fiber optical probe and image algorithms for real time size-shape analysis during crystallization. *Chemical Engineering Science* **2016,** 149, 42-50.
(14) Zhang, R.; Ma, C. Y.; Liu, J. J.; Wang, X. Z., On-line measurement of the real size and shape of crystals in stirred tank crystalliser using non-invasive stereo vision imaging. *Chemical Engineering Science* **2015,** 137, (10), 9-21.
(15) Larsen, P.; Rawlings, J.; Ferrier, N., Model-based object recognition to measure crystal size and shape distributions from in situ video images. *Chemical Engineering Science* **2007,** 62, (5), 1430-1441.
(16) Larsen, P.; Rawlings, J.; Ferrier, N., An algorithm for analyzing noisy, in situ images of high-aspect-ratio crystals to monitor particle size distribution. *Chemical Engineering Science* **2006,** 61, (16), 5236-5248.
(17) Zhang, Y.; Zhang, J.; Jorge, C. A.; Wang, X. Z., Particle shape characterisation and classification using automated microscopy and shape descriptors in batch manufacture of particulate solids. *Particuology* **2016,** 24, (1), 61-68.
(18) Schorsch, S.; Vetter, T.; Mazzotti, M., Measuring multidimensional particle size distributions during crystallization. *Chemical Engineering Science* **2012,** 77, (1), 130-142.
(19) Ma, C. Y.; Liu, J. J.; Wang, X. Z., Measurement, modelling, and closed-loop control of crystal shape distribution: Literature review and future perspectives. *Particuology* **2016,** 26, (3), 1-18.
(20) Zhang, R.; Ma, C. Y.; Liu, J. J.; Zhang, Y.; Liu, Y. J.; Wang, X. Z., Stereo imaging camera model for 3D shape reconstruction of complex crystals and estimation of facet growth kinetics. *Chemical Engineering Science* **2017,** 160, 171-182.
(21) Bujak, B.; Bottlinger, M., Three-dimensional measurement of particle shape. *Particle & Particle Systems Characterization* **2008,** 25, (4), 293-297.
(22) Chakraborty, J.; Sarkar, D.; Singh, A.; Bharti, A. K., Measuring the three-dimensional morphology of crystals using regular reflection of light. *Crystal Growth & Design* **2012,** 12, (12), 6042-6049.
(23) Kempkes, M.; Vetter, T.; Mazzotti, M., Measurement of 3D particle size distributions by stereoscopic imaging. *Chemical Engineering Science* **2010,** 65, (4), 1362-1373.
(24) Schorsch, S.; Ochsenbein, D. R.; Vetter, T.; Morari, M.; Mazzotti, M., High accuracy online measurement of multidimensional particle size distributions during crystallization. *Chemical Engineering Science* **2014,** 105, 155-168.
(25) Borchert, C.; Temmel, E.; Eisenschmidt, H.; Lorenz, H.; Seidel-morgenstern, A.; Sundmacher, K., Image-based in situ identification of face specific crystal growth rates from crystal populations. *Crystal Growth & Design* **2014,** 14, (3), 952–971.
(26) Rajagopalan, A. K.; Schneeberger, J.; Salvatori, F.; Bötschi, S.; Ochsenbein, D. R.; Oswald, M. R.; Pollefeys, M.; Mazzotti, M., A comprehensive shape analysis pipeline for stereoscopic measurements of particulate populations in suspension. *Powder Technology* **2017,** 321, 479-493.

(27) Ma, C. Y.; Liu, J. J.; Wang, X. Z., Stereo imaging of crystal growth. *AIChE Journal* **2016,** 62, (1), 18-25.
(28) Wu, K.; Ma, C. Y.; Liu, J. J.; Zhang, Y.; Wang, X. Z., Measurement of crystal face specific growth kinetics. *Crystal Growth & Design* **2016,** 16, (9), 4855-4868.
(29) Chen, Z.; Liao, H.; Zhang, X., Telecentric stereo micro-vision system: calibration method and experiments. *Optics & Lasers in Engineering* **2014,** 57, 82-92.
(30) Schreier, H. W.; Garcia, D.; Sutton, M. A., Advances in light microscope stereo vision. *Experimental Mechanics* **2004,** 44, (3), 278-288.
(31) Huo, Y.; Liu, T.; Wang, X. Z.; Ma, C. Y.; Ni, X., Online detection of particle agglomeration during solution crystallization by microscopic double-view image analysis. *Industrial & Engineering Chemistry Research* **2017,** 56, 11257-11269.
(32) And, E. S. F.; Davey, R. J., Solution-mediated transformation of α to β l-glutamic acid: rate enhancement due to secondary nucleation. *Crystal Growth & Design* **2004,** 4, (5), 1061–1068.
(33) Gonzales, R. C.; Woods, R. E.; Eddins, S. L., *Digital image processing using MATLAB*. Pearson Prentice Hall: Upper Saddle River, NJ, 2004.
(34) Calderon De Anda, J.; Wang, X. Z.; Roberts, K. J., Multi-scale segmentation image analysis for the in-process monitoring of particle shape with batch crystallisers. *Chemical Engineering Science* **2005,** 60, (4), 1053-1065.
(35) Calderon De Anda, J.; Wang, X. Z.; Lai, X.; Roberts, K. J., Classifying organic crystals via in-process image analysis and the use of monitoring charts to follow polymorphic and morphological changes. *Journal of Process Control* **2005,** 15, (7), 785-797.
(36) Mokhtarian, F.; Suomela, R., Robust image corner detection through curvature scale space. *IEEE Transactions on Pattern Analysis & Machine Intelligence* **1998,** 20, (12), 1376-1381.
(37) Awrangjeb, M.; Lu, G., An improved curvature scale-space corner detector and a robust corner matching approach for transformed image identification. *IEEE Transactions on Image Processing* **2008,** 17, (12), 2425-2441.
(38) Calonder, M.; Lepetit, V.; Strecha, C.; Fua, P. In *BRIEF: binary robust independent elementary features*, European Conference on Computer Vision, Heraklion, 2010; Springer: Heraklion, 2010; pp 778-792.
(39) Acharya, P. K.; Henderson, T. C. In *Parameter estimation and error analysis of range data*, 1988 IEEE International Conference on Robotics and Automation, Philadelphia, 1988; Philadelphia, 1988; pp 1709-1714.
(40) Barequet, G.; Har-Peled, S., Efficiently approximating the minimum-volume bounding box of a point set in three dimensions. *Journal of Algorithms* **2001,** 38, (1), 91-109.
(41) Barber, C. B.; Dobkin, D. P.; Huhdanpaa, H., The quickhull algorithm for convex hulls. *ACM Transactions on Mathematical Software* **1996,** 22, (4), 469-483.
(42) Fang, T. P.; Piegl, L. A., Delaunay triangulation in three dimensions. *Computer Graphics & Applications IEEE* **1995,** 15, (5), 62-69.
(43) Zhang, F.; Liu, T.; Huo, Y.; Guan, R.; Wang, X. Z., Investigation of the operating conditions to morphology evolution of β-l-glutamic acid during seeded cooling crystallization. *Journal of Crystal Growth* **2017,** 469, 136–143.
(44) Bowman, A. W.; Azzalini, A., *Applied smoothing techniques for data analysis*. Oxford University Press: New York, 1997.

Appendix: Derivation of Eq.(11)

From Fig.4a, the following two equations stand according to the common property of two similar triangles,

$$\frac{Z - f_c}{Z} = \frac{b_1 - a_1}{b_1} \tag{A1}$$

$$\frac{Z - f_c}{Z} = \frac{b_2 - a_2}{b_2} \tag{A2}$$

where $f_c = f\cos\theta$ and $b_1 + b_2 = b$.

The above equations can be equivalently transformed into

$$\frac{b_1 - a_1}{Z - f_c} = \frac{b_1}{Z} \tag{A3}$$

$$\frac{b_2 - a_2}{Z - f_c} = \frac{b_2}{Z} \tag{A4}$$

Since $b_1 + b_2 = b$, it can be derived that

$$Z = \frac{bf_c}{a_1 + a_2} \tag{A5}$$

Fig.4b shows the geometric diagram in the left view of camera. According to the sine law, there follows

$$\frac{\sin(90 + \tau_l)}{m_l} = \frac{\sin(90 - \theta - \tau_l)}{x_l} \tag{A6}$$

where $n_l = f\sin\theta$.

It can be derived from (A6) that

$$m_l = \frac{x_l \sin(90 + \tau_l)}{\sin(90 - \theta - \tau_l)} \tag{A7}$$

It can be seen from Fig.4b that

$$a_1 = m_l + n_l \tag{A8}$$

Since Fig.4c shows the geometric diagram in the right view of camera, it follows from the sine law that

$$\frac{\sin(90 - \tau_r)}{m_r} = \frac{\sin(90 - \theta + \tau_r)}{x_r} \tag{A9}$$

where $n_r = f\sin\theta - m_r$.

It can be derived from (A9) that

$$m_r = \frac{x_r \sin(90 - \tau_r)}{\sin(90 - \theta - \tau_r)} \tag{A10}$$

It can be seen from Fig.4c that

$$a_2 = n_r \tag{A11}$$

Therefore,

$$a_1 + a_2 = m_l + n_l + n_r \tag{A12}$$

By substituting (A12) into (A5), it yields

$$Z = \frac{bf\cos\theta}{2f\sin\theta + \dfrac{x_l \sin(90+\tau_l)}{\sin(90-\theta-\tau_l)} + \dfrac{x_r \sin(90-\tau_r)}{\sin(90-\theta+\tau_r)}} \tag{A13}$$

which may be rewritten as

$$Z = \frac{bf\cos\theta}{2f\sin\theta + \dfrac{x_l \cos\tau_l}{\cos(\theta+\tau_l)} - \dfrac{x_r \cos\tau_r}{\cos(\theta-\tau_r)}} \tag{A14}$$

where $\tan\tau_l = x_l / f$, $x_l = \dfrac{\gamma}{\kappa}\left|u_l - L/2\right|$, $\tan\tau_r = x_r / f$, and $x_r = \dfrac{\gamma}{\kappa}\left|u_r - L/2\right|$.

List of Table and Figure Captions

Table 1 Measurement errors on a micro-scale rule with a dip angle of 65°

True length (μm)	500 (B-C)	1000 (A-C)	1500 (A-D)	Averaged relative error (%)
Measured length (μm)	481.18	976.32	1427.83	3.65
Measured dip angle (°)	60.35	61.92	63.28	4.85

Table 2 Comparison of relative measurement errors (%) between the proposed method and a 2D measurement method with reference to offline measurement by an electron microscope

Method	Size	α-form		β-form		Averaged relative error (%)
		Length (μm)	Width (μm)	Length (μm)	Width (μm)	
3DM	Mean	3.28	2.87	4.16	3.73	3.58
	Peak	4.39	3.29	3.08	3.84	
2DM	Mean	7.97	7.48	7.92	4.78	7.19
	Peak	8.25	6.71	8.74	5.63	

Table 3 Volume measurement errors on three different monosodium glutamate particles

Item	Particle 1	Particle 2	Particle 3
Off-line verification (mm^3)	0.462	0.371	0.355
The proposed method (mm^3)	0.419	0.338	0.323
Relative error (%)	9.31	8.89	9.01

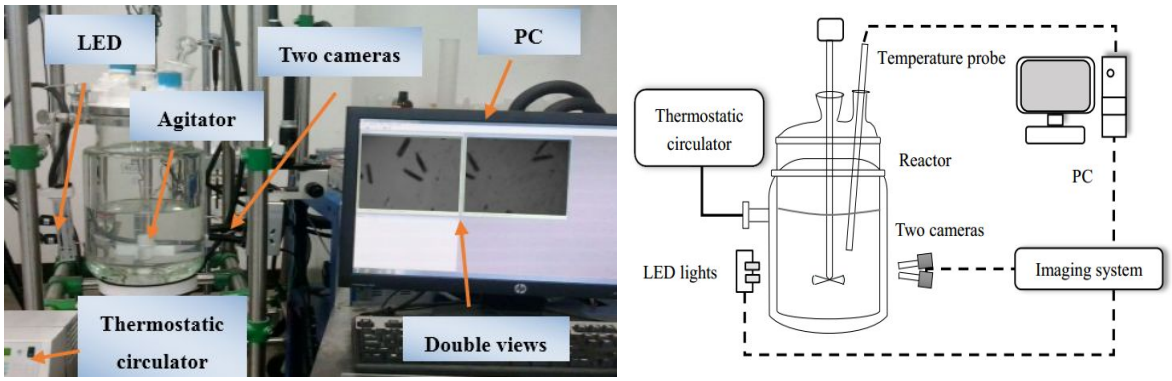

(a) (b)

Fig.1 Non-invasive binocular micro-vision system for monitoring a crystallization process: (a) external view; (b) schematic diagram.

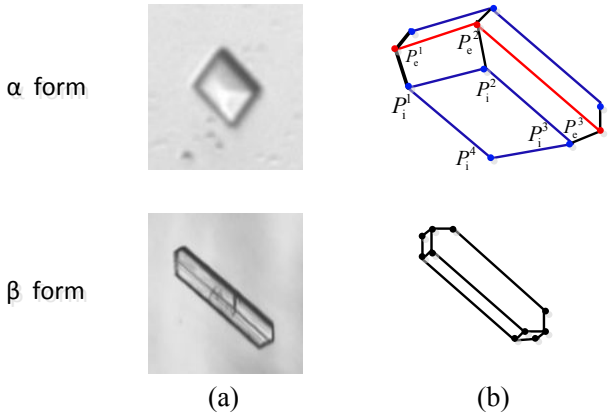

Fig.2 LGA crystal morphologies of α- and β-forms: (a) crystal images; (b) simplified reconstructions (external contour edges are marked in red and internal contour edges are marked in blue for α form).

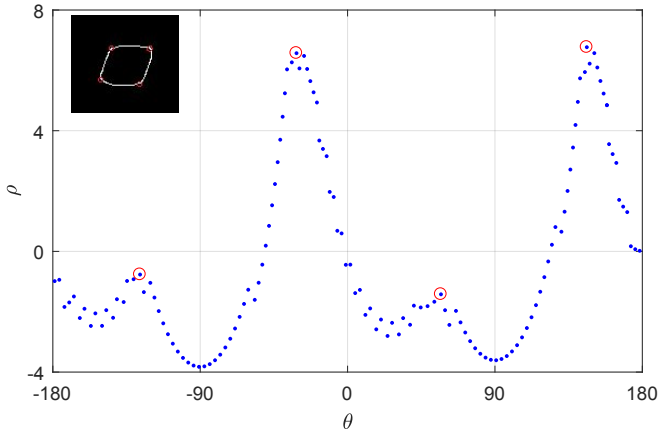

Fig.3 Plot of the inner distances of contour points in an α-form crystal image (The contour image is in the top left corner and the extremum points are marked in red).

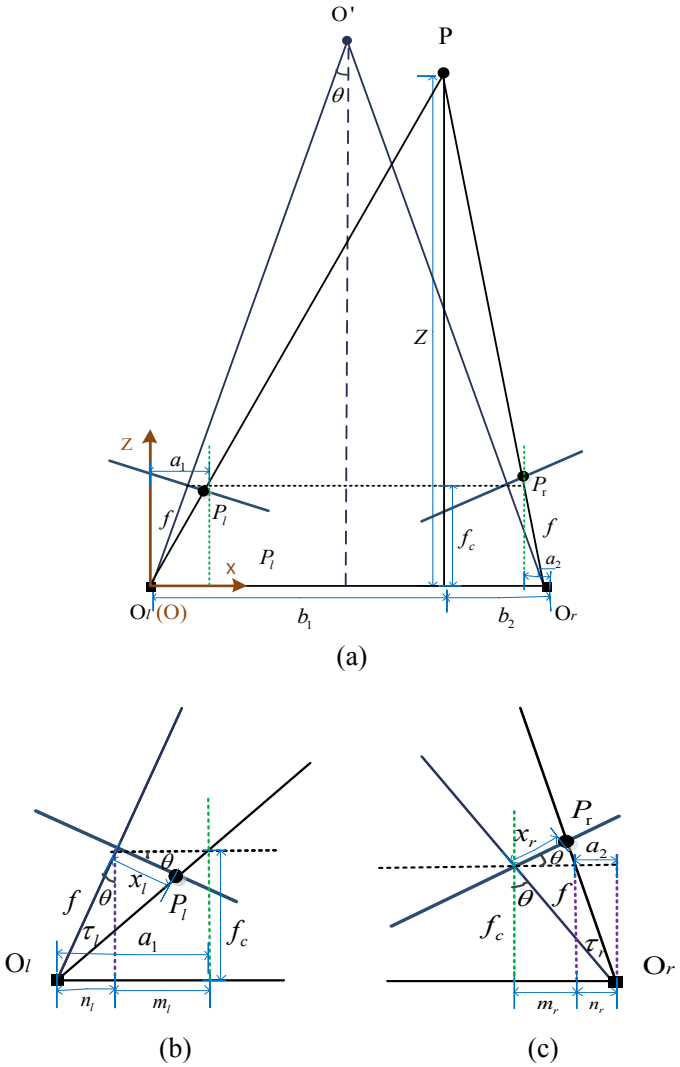

Fig.4 The geometry model of a stereo imaging system: (a) stereo imaging; (b) the left-view model; (c) the right-view model.

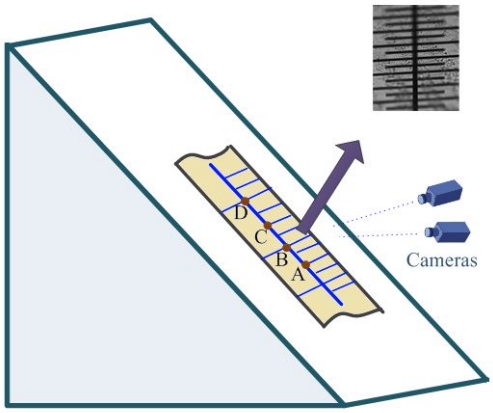

Fig.5 Schematic diagram of the measurement test on a micro-scale ruler.

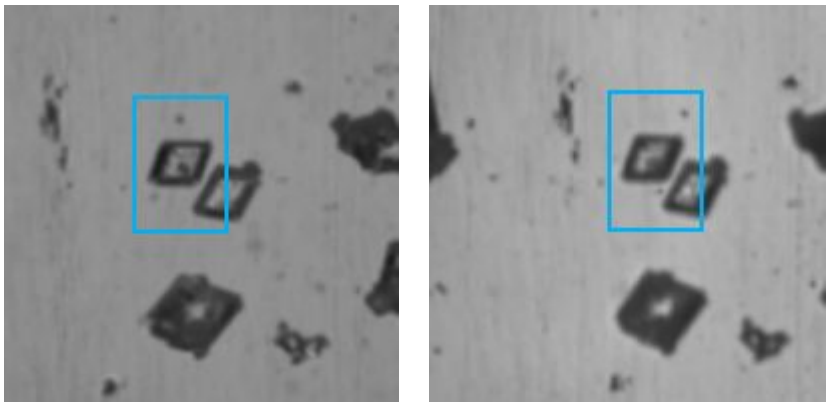

(a)

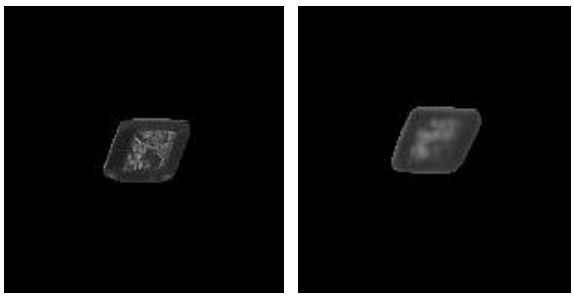

(b)

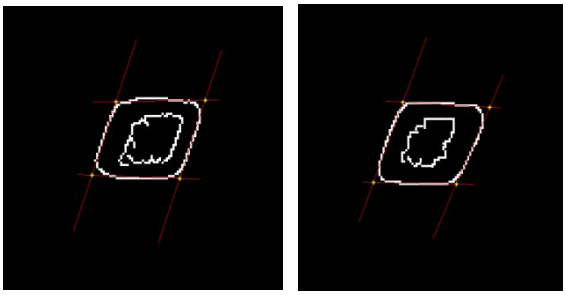

(c)

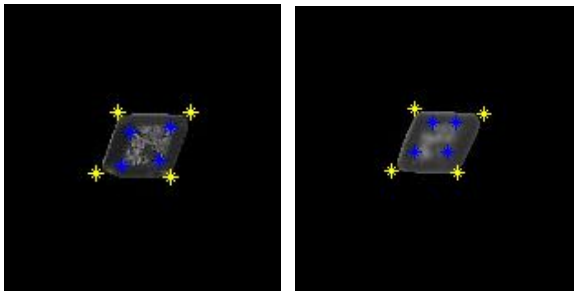

(d)

Fig.6 Image processing results for α-form LGA crystals: (a) original double-view images; (b) segmented double-view images for a sampled crystal; (c) external and internal contours; (d) the key corners.

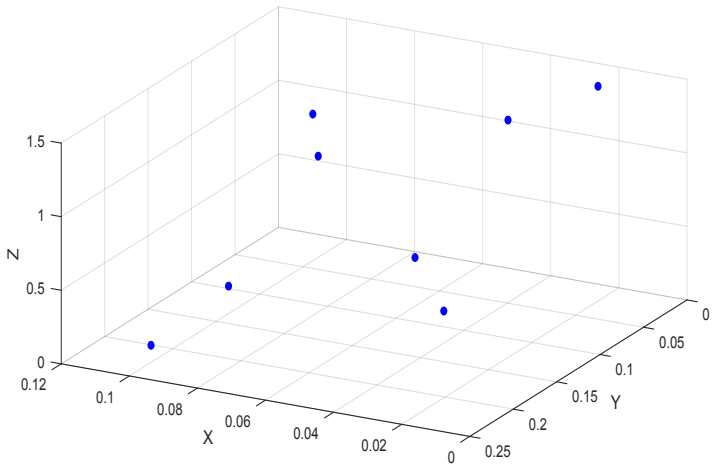

(a)

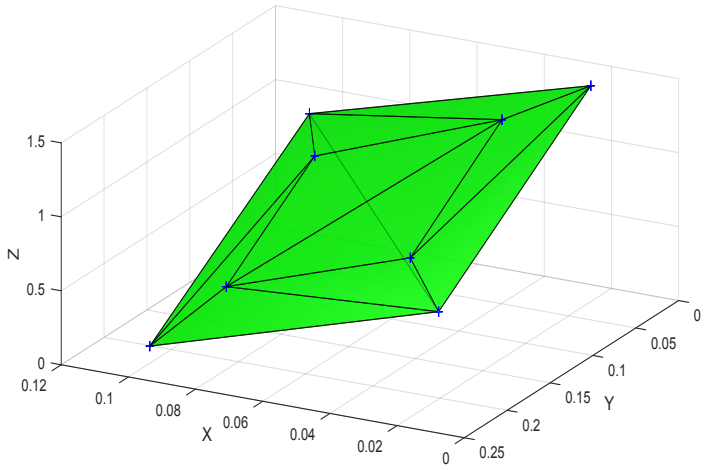

(b)

Fig.7 3D shape reconstruction for an α-form LGA crystal: (a) 3D locations of the key corners; (b) 3D shape reconstruction.

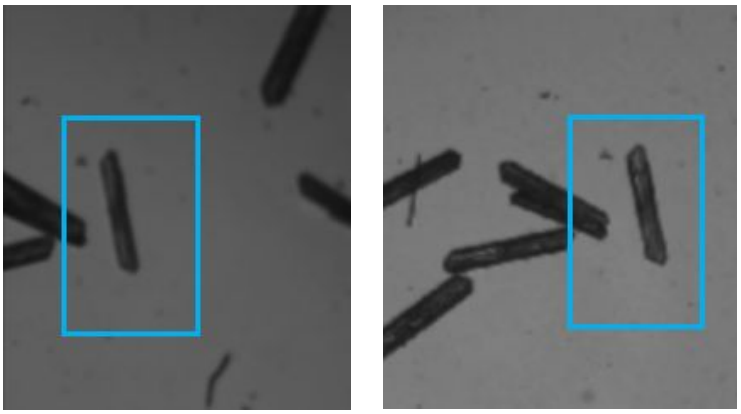

(a)

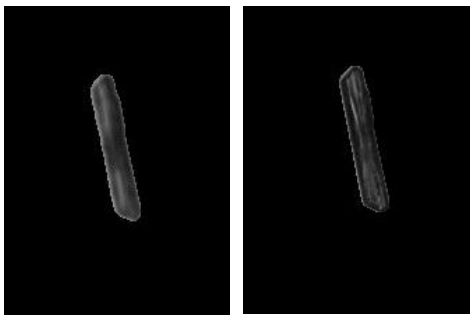

(b)

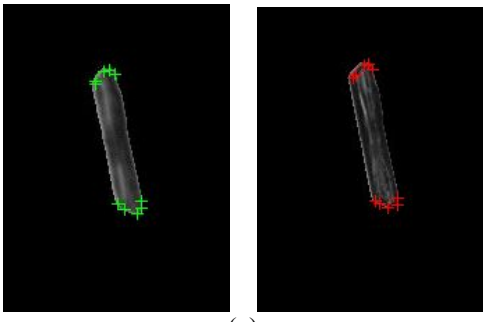

(c)

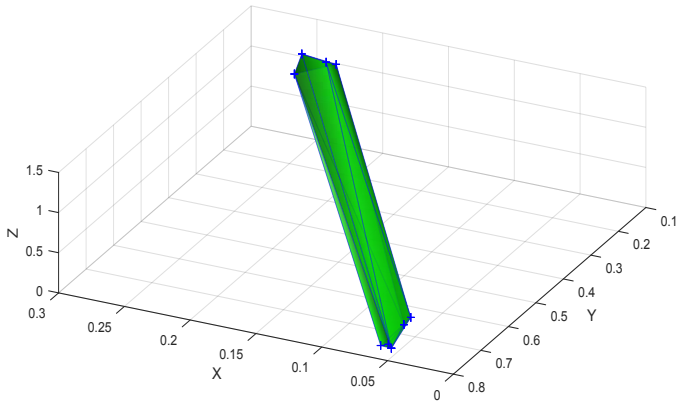

(d)

Fig.8 Illustration of image processing and 3D reconstruction results for a β-form LGA crystal: (a) original double-view images; (b) segmented double-view images for a sampled crystal; (c) key corner detection; (d) 3D shape reconstruction.

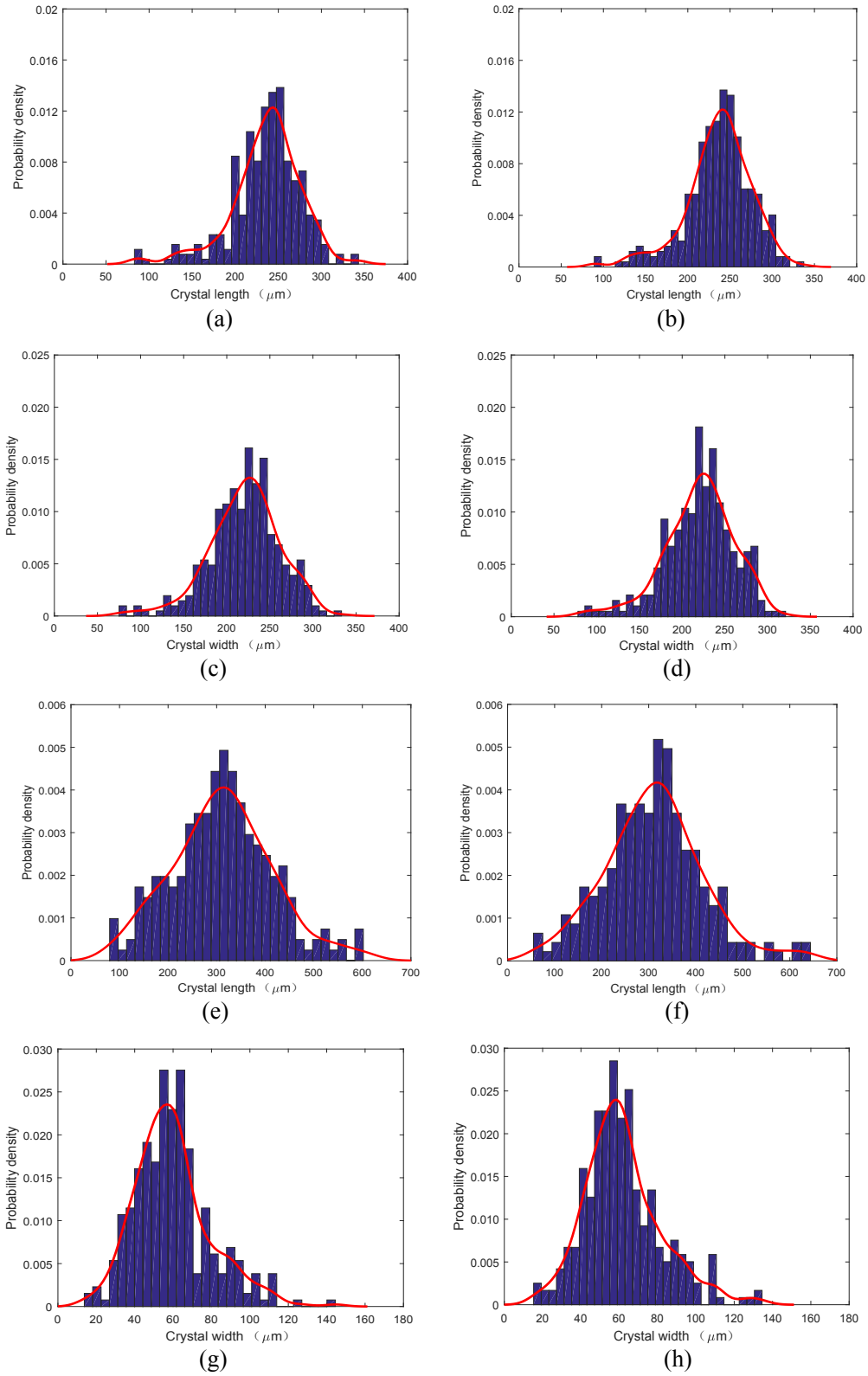

Fig.9 In-situ measured results of LGA CSD compared to off-line measurement by an electron microscope: (a) the length distribution of α-form LGA by the proposed method; (b) the length distribution of α-form LGA by off-line measurement of microscopy; (c) the width distribution of α-form LGA by the proposed method; (d) the width distribution of α-form LGA by off-line measurement of microscopy; (e) the length distribution of β-form LGA by the proposed method; (f) the length distribution of β-form LGA by off-line measurement of microscopy; (g) the width distribution of β-form LGA by the proposed method; (h) the width distribution of β-form LGA by off-line measurement of microscopy.

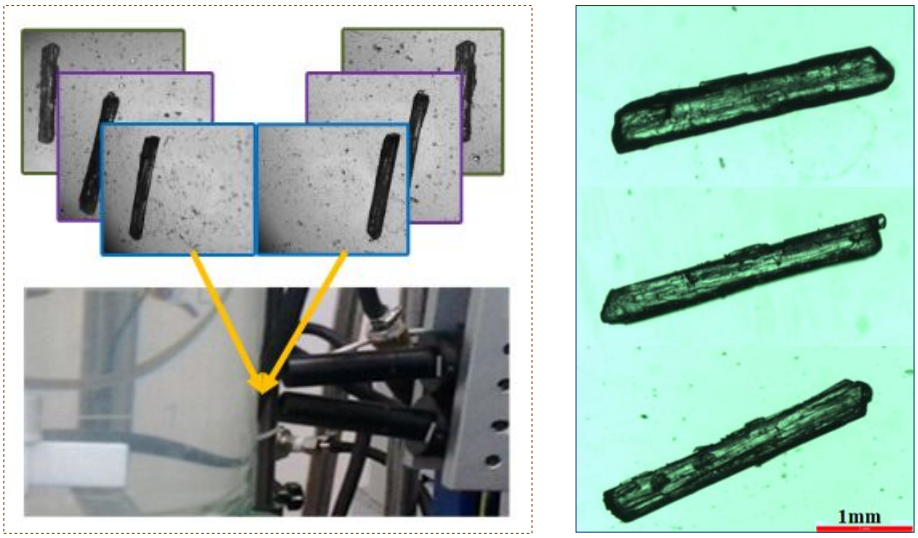

(a) (b)

Fig.10 Experimental verification on volume computation via monosodium glutamate particles: (a) the proposed method based on in-situ double-view imaging; (b) off-line measurement on three different monosodium glutamate crystals by an electron microscope.

In-situ Measurement of 3D Crystal Size Distribution by Double-View Image Analysis with Case Study on L-glutamic Acid Crystallization

Yan Huo [a,b,c], Tao Liu [a,b,*], Yixuan Yang [a,b], Cai Y. Ma [d], Xue Z. Wang [d, e]

[a]*Key Laboratory of Intelligent Control and Optimization for Industrial Equipment of Ministry of Education, Dalian 116024, China*

[b]*Institute of Advanced Control Technology, Dalian University of Technology, Dalian 116024, China*

[c]*College of Information Engineering, Shenyang University, Shenyang 110044, China*

[d]*Institute of Particle Science and Engineering, School of Chemical and Process Engineering, University of Leeds, Leeds LS2 9JT, UK*

[e]*School of Chemistry and Chemical Engineering, South China University of Technology, Guangzhou 510006, China*

** Corresponding author. Tel: +86-411-84706465; Fax: +86-411-84706706; E-mail: liurouter@ieee.org*

Abstract: In this paper, an in-situ measurement method is proposed for monitoring three-dimensional (3D) crystal size distribution (CSD) during a crystallization process, based on a binocular micro-vision system. The stereo particle shape is reconstructed from double-view images captured by two microscopic cameras fixed at different angles outside the crystallizer. To overcome the influence from solution turbulence and uneven illumination background involved with in-situ imaging, a microscopic double-view image analysis method is established to identify the key corners of each particle shape in the captured images, including corner detection and corner matching. Two fast algorithms are therefore given for on-line detection of two typical crystal morphologies of prismatic and needle-like shapes, such as α- and β-forms of L-glutamic acid (LGA) crystals, respectively. Based on the identified key corners for different particle shapes, a 3D geometry model is established to approximately reconstruct the 3D shape for each imaged particle, such that 3D sizes of each particle could be quantitatively estimated, along with the particle volume. Experiments on the LGA cooling crystallization are performed to demonstrate the effectiveness of the proposed method.

Keywords: Crystal size distribution, three-dimensional (3D) particle size measurement, binocular micro-vision system, 3D geometry reconstruction, corner detection, L-glutamic acid crystallization.

1. Introduction

The crystallization technology has been widely used for separating different components from solution and purifying particle products in chemical and pharmaceutical industries. For control and optimization of crystallization processes, on-line process analytical technologies (PATs) have been explored for assessing the crystal morphology, growth rate and quality [1-4]. With a rapid development of the photoelectric technology, on-line image based monitoring methods were increasingly studied for measuring the sizes and shape of crystals [5-9]. Based on image analysis of multi-dimensional crystal sizes and shape feature, a few crystal morphology analysis methods were developed for monitoring the crystal quality during crystallization [10, 11]. The developed imaging systems for monitoring crystallization processes mainly include two types: invasive and non-invasive. For using an invasive imaging system, e.g., the digital particle vision and measurement (PVM) [12] , the imaging probe could be stuck into the crystal slurry to capture the crystal images. A novel invasive imaging probe was recently developed based on the existing image analysis methods to cope with blurry images with noise [13]. In contrast, a non-invasive imaging system is installed outside a crystallizer to image the crystallization process by the observation window [14, 15]. Compared with an invasive imaging system, a non-invasive imaging system could avoid the contamination of camera lens from the crystal slurry. However, the lighting source of a non-invasive imaging system needs to be carefully installed in an opposite position to the cameras outside the crystallizer, in order to provide sufficient illumination for real-time imaging.

With crystal images captured by an invasive or non-invasive imaging system, Larsen et al. [16] developed an efficient image processing algorithm for analyzing the crystal size distribution (CSD) of high-aspect-ratio crystals. Zhang et al. [17] proposed a few particle shape descriptors based on the principal component analysis (PCA) to classify polymorphic organic crystals during batch crystallization. A synthetic image analysis method [11] was recently presented for in-situ crystal size measurement and shape identification. Gao et al. [8] proposed an in-situ measurement method based on the recently developed deep learning technology to classify α- and β-forms of L-glutamic acid (LGA) crystals and measure the two-dimensional (2D) sizes of length and width, along with an estimation of the surface area. This approach needs a large amount of samples of α- or β-form

crystals for off-line training along with a demanding computation effort. For monitoring the crystal growth quality, it was pointed out that 2D image analysis methods could provide relatively less information than those of 3D imaging methods [18-20]. Bujak and Bottlinger [21] adopted three orthogonally installed cameras to measure 3D sizes of particles with irregular shapes, but not for imaging crystals in the slurry. An off-line 3D shape measurement method was developed based on assembling the 2D surface images of a crystal captured by using a regular reflection of light [22]. Another off-line 3D size measurement method [23] was proposed for cuboid crystals such as β-form LGA, by using a multi-projection imaging system consisting of one camera and two mirrors. This approach was subsequently extended for on-line measurement by imaging a flow through cell using a sampling loop with two external cameras installed orthogonal to each other [24], which was mainly devoted to cuboid crystals. Borchert et al. [25] developed an alternative image analysis method for reconstructing the 3D crystal shape from the corresponding 2D crystal projections, where the Fourier descriptors were used to detect the crystal shape outline based on a pre-defined database of different crystal shapes. Recently, a new dual-camera measurement device was developed for real-time monitoring of particle shapes rather than 3D size measurement via a circulating pipeline [26], based on an image segmentation algorithm for background extraction and a volume intersection method for classification of different 3D particle shapes. Ma et al. [27] presented a proof-of-concept of 3D shape reconstruction based on using two no-invasive cameras installed with a pre-specified angle to synchronously capture images, which was further extended in the references [20, 28] for roughly estimating 3D size growth of crystals rather than quantitative measurement. For using a binocular micro-vision system to capture stereo images for analysis, a few calibration methods for guaranteeing the measurement accuracy were reported in the references [29, 30], but these methods could not be used for in-situ installed micro-vision systems subject to uneven illumination background, particle motion, and solution turbulence usually involved with crystallization processes. Although the recent work [31] developed a microscopic double-view image analysis method for in-situ measurement of 2D particle sizes, it remains open to measure the third dimensional particle size that could be perpendicular to the 2D imaging plane, and therefore, the particle volume could not be estimated therein.

To tackle the difficulty of measuring 3D sizes and volumes of particles during crystallization, an in-situ image-based measurement method is proposed in this paper with application to the cooling crystallization processes of α- and β-form LGA crystals, based on a non-invasive binocular micro-vision system. Firstly, two fast image analysis algorithms are given for identifying the key corners of two typical crystal morphologies, i.e., prismatic α-form and needle-like β-form of LGA crystals, respectively. Then, a binocular geometric model is constructed for computing the 3D space location of each corner. Based on the computed 3D coordinates of these key corners, a 3D geometry model is established to approximately reconstruct the 3D particle shape, which is therefore used for measuring the 3D sizes of each particle in the in-situ captured images. A measurement test on a micro-scale ruler placed in 3D location is conducted to verify the accuracy of the proposed method for 3D size measurement. In addition, another fast algorithm is given for computing the volumes of particles with image reconstruction, for the convenience of real-time application. Experiments on monitoring the cooling crystallization process of LGA are performed to demonstrate the effectiveness of the proposed method for in-situ measurement of particle sizes.

2. Experimental set-up

2.1 Non-invasive binocular micro-vision system for in-situ measurement

The experimental set-up for using a non-invasive binocular vision system to monitor a cooling crystallization process is shown in Fig.1, where the crystallizer consists of a 4L jacketed glass reactor (ACE-AIO 4000), a 4-paddle agitator (PTFE), a thermostatic circulator (Julabo-CF41), and a temperature probe (Pt100). The non-invasive binocular vision system for in-situ imaging during crystallization was made by Hainan Six Sigma Intelligent Systems Ltd. (product no. Stereo Vision Crystal-G), which consists of two microscopic cameras and two lighting sources commanded by a light controller (Gardasoft RT260-20) for snapshot. Each camera has a CCD sensor with the maximum pixel resolution of 2448×2048 and a micro lens set at a distance of 40mm from the reactor glass wall (the maximum working distance is about 65mm). The maximum frame rate is 6.5 fps for each camera. For in-situ measurement, two microscopic cameras are situated up and down in a line outside the glass vessel so as to alleviate the distortion for capturing images, while

there is an intersection angle of 12.5 degree between the optical axes of two cameras. The lighting sources are installed in line with the camera lens on the other side of the glass vessel, providing the lighting illumination of 350lux. For real-time analysis, a pair of microscopic images is synchronously shot via two cameras per two seconds during the crystallization process.

2.2 Crystallization material of LGA

The solute material used in this study is LGA ($C_5H_9NO_4$). LGA has two typical polymorphic forms [5, 32], prismatic α-form and needle-like β-form, as shown in Fig.2. Different linear cooling rates [5] were studied to procure these two product forms. In this work, the LGA solution was taken as distilled water.

To perform a cooling crystallization experiment of LGA, the solution is initially heated up to 70°C and then maintained at the temperature until all the LGA solute is completely dissolved. After that, the solution is cooled down to 20°C by a specified cooling rate and maintained at the temperature until the end of experiment. The agitator is operated at a constant rate of 200 rpm to maintain the uniformity of particle distribution in the suspension during crystallization.

3. Double-view image analysis on the key corners of particle shapes

Since double-view images in-situ captured by a non-invasive binocular vision system shown in Fig.1 were blurred by solution turbulence and uneven illumination background, it is necessary to identify salient features of particle shapes in these images for analyzing 3D particle morphology and sizes. To exclude the noise affect, the well-known median filter [33] may be used to recover the denoised grayscale images from the captured images for real-time analysis. Then, a multi-scale segmentation with the Canny operator [34] is preferred to detect the particle shape edge from a denoised image. Note that any unobvious edge points could be removed by using a specified threshold. By filling the gaps between identified edge points with their adjacent edge features, the contour edge of each particle image could be determined in an efficient manner.

For reconstructing 3D particle shapes based on the pre-processed images to measure the particle 3D sizes, it is proposed to detect the key corners of each particle. LGA crystals have two typical polymorphic forms, prismatic α-form and needle-like β-form [8, 35], as shown in Fig.2a. Note

that these two shapes could be distinguished from in-situ captured images by using the inner distance descriptor introduced in the previous work [11]. However, their key corners are distinct from each other in the geometric location for shape reconstruction, as shown in Fig.2b. Concerning an α-form crystal, the 3D image contour after edge detection includes external and internal edges, and correspondingly, there are eight key corners to be detected, including four external and internal key corners, respectively. In contrast, a β-form crystal has a needle-like shape where the key corners are located at both ends of the image contour. Two different algorithms are therefore proposed to detect the key corners of α- and β-form crystals, respectively.

For detecting the key corners of an α-form crystal, the coordinates of all the contour points are denoted by (x_n, y_n), where $n = 1, 2, \ldots, N$, and therefore, the centroid coordinate denoted by (x_c, y_c) is defined by

$$\begin{cases} x_c = \dfrac{1}{N}\sum_{n=0}^{N-1} x_n \\ y_c = \dfrac{1}{N}\sum_{n=0}^{N-1} y_n \end{cases} \tag{1}$$

Correspondingly, the inner distances from the centroid to the boundary points are defined by

$$d_n = \sqrt{(x_c - x_n)^2 + (y_c - y_n)^2} \tag{2}$$

The inner distances of all the contour points are plotted in Fig.3, where the peak points are defined as the extremum points of the contour. The set of each edge point is composed of the boundary points between every two edge extreme points. The fitting lines $y = a_j x + b_j$, $j = 1, \ldots, 4$ along each edge are optimized by a least-squares (LS) algorithm as

$$\begin{cases} a_j = \dfrac{1}{C^j}\sum_{k=1}^{K} ({x_k}^j - \bar{x}^j)({y_k}^j - \bar{y}^j) \\ b_j = \bar{y}^j - a_j \bar{x}^j \end{cases} \tag{3}$$

where $C^j = \sum_{k=1}^{K} ({x_k}^j - \bar{x}^j)^2$, and K is the point number.

The key corners of either external or internal contour edges are determined by computing the crossover points of the above fitting lines. Note that the external and internal key corners are detected for determining the external and internal contour edges, respectively, as shown in Fig.2b.

For clarity, the proposed corner detection algorithm for prismatic α-form crystals is

summarized below.

Step 1: Find the external or internal contour edges using the Canny edge detector;

Step 2: Define the extremum points of external or internal contour edges in a particle image, by computing the centroid coordinates of the external or internal contour edges via Eq.(1) and the inner distances of all the contour points via Eq.(2), and then choosing the peak points in the plot of the inner distances;

Step 3: Fit the external contour edges in a particle image by optimizing the fitting lines along each edge via Eq.(3);

Step 4: Determine the external and internal key corners by computing the crossover points of the above fitting lines.

For detecting the key corners of a β-form crystal, the candidate corners are selected based on the curvature scale-space method that has good robustness against noise [36, 37]. For the particle contour described by $\psi(u)=\left(x(u),y(u)\right)$, where u denotes the length parameter, the corresponding multi-scale curve $\psi(u,\sigma)$ under a scale σ is defined by

$$\psi(u,\sigma)=\left(X(u,\sigma),Y(u,\sigma)\right) \tag{4}$$

where

$$\begin{cases} X(u,\sigma)=x(u)*g(u,\sigma) \\ Y(u,\sigma)=y(u)*g(u,\sigma) \end{cases} \tag{5}$$

where $*$ denotes the convolution operator, and $g(u,\sigma)$ denotes a Gaussian function with the standard deviation σ.

The curvature of $\psi(u,\sigma)$ is computed by

$$\psi(u,\sigma)=\frac{X_u(u,\sigma)Y_{uu}(u,\sigma)-X_{uu}(u,\sigma)Y_u(u,\sigma)}{\left(X(u,\sigma)^2+Y(u,\sigma)^2\right)^{1.5}} \tag{6}$$

where $X_u(u,\sigma)$ and $X_{uu}(u,\sigma)$ are the first and second order derivatives of $X(u,\sigma)$ with respect to u. $Y_u(u,\sigma)$ and $Y_{uu}(u,\sigma)$ are the first and second order derivatives of $Y(u,\sigma)$ with respect to u.

According to Eq.(6), the curvature $\psi(u,\sigma_j)$ of an edge point on the scale j can be

computed, and then the curvature product at four different scales is computed as

$$\Gamma(u) = \prod_{j=1}^{4} \psi(u, \sigma_j) \tag{7}$$

Subsequently, a local maximum edge point with a curvature product greater than a specified threshold, e.g., $T = 0.03$ given in the reference [37] for corner detection, is taken as a candidate corner. Considering that corner points should be at both ends of the crystal shape as shown in Fig.2b, the key corners are determined by specifying a criterion, i.e., the inner distance of a candidate corner should be no less than one third of the crystal length.

Hence, the proposed corner detection algorithm for need-like β-form crystals is summarized below.

Step 1: Find the external contour edges using the Canny edge detector;

Step 2: Define the corners of the contour edges in a particle image by the curvature scale-space approach using Eqs.(4-7);

Step 3: Exclude those corners not complying with the inner distance criterion.

After the key corner detection, matching the key corners between double-view images is conducted by using the BRIEF descriptor [38] owing to its robustness and fast speed for real-time application. To determine the descriptor, a square region I of size $S \times S$ (i.e., pixel number) is chosen around such a key corner. Denote by p_i and q_i two different pixel points located in I, where i is the pixel index and N is 256. To avoid sensitivity to noise, each region is preprocessed by the Gaussian smoothing approach [38]. Then, an N-bit vector denoting the BRIEF descriptor is defined by

$$b_N(I) = \sum_{1 \le i \le N} 2^{i-1} g(I; p_i, q_i) \tag{8}$$

where

$$g(I; p_i, q_i) = \begin{cases} 1 & if\ I(p_i) < I(q_i) \\ 0 & \text{otherwise} \end{cases} \tag{9}$$

where $I(p_i)$ and $I(q_i)$ are the intensities of p_i and q_i in the region I. Note that (p_i, q_i) follow the Gaussian distribution of $(0, 1/25S^2)$.

The similarity between corner descriptors computed from double-view images is then measured by the Hamming distance [38], which determines the matching pairs of key corners in double-view images in terms of the maximum similarity degree.

It should be noted that the quality of particle morphology reconstruction depends on the identified key corners, which is affected by 3D location of each particle in the captured images.

4. Stereo shape reconstruction and measurement of 3D particle sizes

Based on the identified key corners in double-view images, a 3D geometry model is proposed to approximately reconstruct the stereo shape of each particle appearing in double-view images. Correspondingly, the 3D sizes and volume of each particle are measured based on the established 3D geometry model. An error analysis is given to verify the accuracy of the proposed method, along with an experiment on measuring a micro-scale ruler by using the non-invasive binocular micro-vision system shown in Fig.1.

4.1 3D geometry model

Fig.4a shows a geometry model case of imaging a space point denoted by P with the non-invasive binocular micro-vision system shown in Fig.1, where the left-view and right-view images are captured from the installed upper and lower cameras, respectively. The model origin of the 3D coordinate system is set to the left-view centroid as shown in Fig.4a, denoted by O. For 3D shape reconstruction, the 3D coordinate (X,Y,Z) of a space point P is a function of the 2D coordinates denoted by P_l and P_r in the double-view projections. Denote by $P_l(u_l,v_l)$ and $P_r(u_r,v_r)$ the imaging points from the left-view and right-view, respectively, both of which have the same size of $L\times H$ (length × height) with P. Denote by γ the pixel equivalent without amplification, by κ the amplification coefficient, by b the baseline length, and by 2θ, ($0<\theta<90^\circ$) the stereo angle.

Without loss of generality, the 3D coordinate (X,Y,Z) of P is derived as

$$\begin{cases} X = Z\tan(\theta + p\tau_l) \\ Y = \gamma(v_l - H/2) \\ Z = bf\cos\theta/(2f\sin\theta + a_l + a_r) \end{cases} \tag{10}$$

Correspondingly, the key parameters of a_l and a_r in Eq.(10) that depend on the locations of point projection (i.e. u_l and u_r) in these images are derived as

$$a_l = p\frac{x_l \cos\tau_l}{\cos(\tau_l + p\theta)} \tag{11}$$

$$a_r = q\frac{x_r \cos\tau_r}{\cos(\tau_r + q\theta)} \tag{12}$$

with

$$p = \begin{cases} 1, & u_l \geq L/2 \\ -1, & u_l < L/2 \end{cases} \tag{13}$$

$$q = \begin{cases} -1, & u_r \geq L/2 \\ 1, & u_r < L/2 \end{cases} \tag{14}$$

where $\tan\tau_l = x_l / f$, $x_l = \frac{\gamma}{\kappa}|u_l - L/2|$, $\tan\tau_r = x_r / f$, $x_r = \frac{\gamma}{\kappa}|u_r - L/2|$.

For comprehension, a brief derivation of Eq.(10) for the case of $u_l \geq L/2$ and $u_r \geq L/2$ as shown in Fig.4a, is given in the Appendix. Similarly, the computational formulae of the 3D coordinate (X,Y,Z) of a space point P can be derived for the other three cases, $u_l \geq L/2$ and $u_r < L/2$; $u_l < L/2$ and $u_r \geq L/2$; $u_l < L/2$ and $u_r < L/2$, which are omitted for brevity.

Hence, the 3D coordinates of all the key corners in the image contour of each particle can be computed, and therefore, are used to approximately reconstruct the 3D geometry model of each particle shape, as shown in Fig.2.

4.2 Measurement error analysis

The derivation in the above section indicates that the 3D coordinates of key corners depend on the structural parameters of the non-invasive binocular micro-vision system shown in Fig.1, i.e., the pixel equivalent and the location of the image points. The 3D coordinate of such a space point can be expressed as a vector function,

$$(X,Y,Z) = F(f,b,\theta,\gamma,u_l,u_r) \tag{15}$$

It is therefore seen that the measurement error arises from the structural parameter error ($\Delta f, \Delta b, \Delta\theta$), the size calibration error $\Delta\gamma$, and the image corner extraction error ($\Delta u_l, \Delta u_r$). In fact, the structural parameter error could be negligible or reduced to a very small value if the non-invasive binocular micro-vision system is properly installed. Therefore, the size calibration error

and image corner extraction error should be mainly considered to ensure the 3D measurement accuracy. It should be noted that the size calibration error is affected by the imaging object distance. Hence, different pixel equivalent values should be taken into account with respect to different imaging object distances, especially for a large depth-of-field imaging system.

Verification of the measurement error is necessary for practical application. However, few references addressed feasible verification methods for micro-scale particle size measurement. It remains open as yet to verify the accuracy and reliability of measuring 2D or 3D particle sizes by using a micro-vision system. To tackle the difficulty, two critical indices including the space size and dip angle are therefore introduced for assessing accuracy of the reconstructed stereo shape for an imaged particle. Note that the dip angle is a 3D index which is not needed for 2D measurement. In this study, a linear micro-scale ruler is used for experimental verification, in consideration of that different sizes can be directly exemplified in micro-scale. Meanwhile, a geometric holder is used to provide a dip angle of 65^{o} for placing the micro-scale ruler to conduct 3D measurement. Fig.5 shows a schematic diagram of the experimental verification. The measurement results for the line segments from point B to point C (denoted by B-C), from point A to point C (denoted by A-C) and from point A to point D (denoted by A-D) are listed in Table 1, where the relative measurement error is defined by

$$E = |a - b| / b \times 100\% \tag{16}$$

where a is the measured value, and b is the true value.

It is seen that the averaged relative error for measuring these segments is smaller than 5%, while the averaged relative error for measuring the dip angle is only about 5%, well demonstrating good accuracy of the proposed 3D measurement method. Note that if the structural parameters of the imaging system could be measured more precisely, the relative error will be further reduced.

4.3 Measurement of 3D sizes and particle volume

The reconstructed 3D geometry model for each particle is used to measure the 3D sizes (namely, length, width and height) and particle volume. In view of that the 3D shapes for α- and β-form particles are obviously different from each other, as shown in Fig.2, the corresponding measurement algorithms are proposed below, respectively.

For an α-form particle, it is seen from Fig.2b that there are four external and internal key corners, respectively. Denote the external corner points by $\{P_{\mathrm{e}}^{n}(x_{\mathrm{e}}^{n}, y_{\mathrm{e}}^{n}, z_{\mathrm{e}}^{n}), n=1,2,3,4\}$ and the internal corner points by $\{P_{\mathrm{i}}^{n}(x_{\mathrm{i}}^{n}, y_{\mathrm{i}}^{n}, z_{\mathrm{i}}^{n}),\ n=1,2,3,4\}$. To describe the length of the reconstructed 3D geometry model, the length of α-form particle is computed as

$$S_{\mathrm{l}} = \max(d_{\mathrm{l}}^{n}),\ \ n=1,2,3,4 \tag{17}$$

where d_{l}^{n}, $n=1,2,3,4$ denote the line segment lengths $D(P_{\mathrm{e}}^{1}, P_{\mathrm{e}}^{2})$, $D(P_{\mathrm{e}}^{2}, P_{\mathrm{e}}^{3})$, $D(P_{\mathrm{e}}^{3}, P_{\mathrm{e}}^{4})$ and $D(P_{\mathrm{e}}^{4}, P_{\mathrm{e}}^{1})$, respectively.

Correspondingly, the width of α-form particle is computed as

$$S_{\mathrm{w}} = \min(d_{\mathrm{w}}{}^{n}),\ \ n=1,2,3,4 \tag{18}$$

where $d_{\mathrm{w}}{}^{n}$, $n=1,2,3,4$ denotes the distances between P_{e}^{1} and the line segment $P_{\mathrm{e}}^{3}P_{\mathrm{e}}^{4}$, P_{e}^{2} and the line segment $P_{\mathrm{e}}^{1}P_{\mathrm{e}}^{4}$, P_{e}^{3} and the line segment $P_{\mathrm{e}}^{1}P_{\mathrm{e}}^{2}$, P_{e}^{4} and the line segment $P_{\mathrm{e}}^{2}P_{\mathrm{e}}^{3}$, respectively.

To compute the height of the reconstructed 3D geometry model, two fitting planes of the external and internal corner points are constructed, respectively. Suppose a fitting plane expressed by $ax+by+cz=d$, where a, b, c are unit normal vectors of the plane, satisfying $a^2+b^2+c^2=1$ and $d\geq 0$. For four space points denoted by $\{P_n(x_n, y_n, z_n), n=1,2,3,4\}$, a recognized optimization program [39] for determining the fitting plane parameters (a,b,c,d) can be used,

$$\min_{a,b,c,d} \sum_{n=1}^{4} (ax_n + bx_n + cz_n - d)^2 \tag{19}$$

To solve the above optimal program, let $s_n = | ax_n + by_n + cz_n - d |$ and a penalty function with the Lagrange multiplier is defined by

$$f = \sum_{n=1}^{4} s_n{}^2 - \lambda(a^2+b^2+c^2-1) \tag{20}$$

The derivative of Eq.(20) with respect to d is obtained as

$$\frac{\partial f}{\partial d} = -2\sum_{n=1}^{4} (ax_n + bx_n + cz_n - d) \tag{21}$$

By letting (21) be zero, it yields

$$d = a\frac{\sum_{n=1}^{4} x_n}{4} + b\frac{\sum_{n=1}^{4} y_n}{4} + c\frac{\sum_{n=1}^{4} z_n}{4} \tag{22}$$

Similarly, by letting the derivative of Eq. (20) with respect to a, b, c be zero, respectively, there follows

$$\begin{cases} \sum_{n=1}^{4}(a\Delta x_n + b\Delta x_n + c\Delta z_n)\Delta x_n - \lambda a = 0 \\ \sum_{n=1}^{4}(a\Delta x_n + b\Delta x_n + c\Delta z_n)\Delta y_n - \lambda b = 0 \\ \sum_{n=1}^{4}(a\Delta x_n + b\Delta x_n + c\Delta z_n)\Delta z_n - \lambda c = 0 \end{cases} \tag{23}$$

where $\Delta x_n = x_n - \bar{x}_n$, $\Delta y_n = y_n - \bar{y}_n$, and $\Delta z_n = z_n - \bar{z}_n$.

The eigenvalue equation of Eq.(23) is defined by

$$\boldsymbol{A}\boldsymbol{x} = \lambda \boldsymbol{x} \tag{24}$$

where

$$\boldsymbol{x} = (a, b, c)^T \tag{25}$$

$$\boldsymbol{A} = \begin{bmatrix} \Delta x_n \Delta x_n & \Delta x_n \Delta y_n & \Delta x_n \Delta z_n \\ \Delta x_n \Delta y_n & \Delta y_n \Delta y_n & \Delta y_n \Delta z_n \\ \Delta x_n \Delta z_n & \Delta y_n \Delta z_n & \Delta z_n \Delta z_n \end{bmatrix} \tag{26}$$

The eigenvalue value of Eq.(24) can be solved as

$$\lambda = \frac{(\boldsymbol{A}\boldsymbol{x}, \boldsymbol{x})}{(\boldsymbol{x}, \boldsymbol{x})} = \sum_{n=1}^{4}(a\Delta x_n + b\Delta x_n + c\Delta z_n)^2 = \sum_{n=1}^{4} {s_n}^2 \tag{27}$$

where $(,)$ denotes the inner product of two vectors.

The minimum of $\sum_{n=1}^{4} {s_n}^2$ corresponds to the smallest eigenvalue of $\boldsymbol{A}$, which therefore determines the optimal eigenvector (a, b, c). Hence, the optimal fitting planes of the external and internal corner points could be determined, respectively.

Considering that the fitting plane of the external corner points may not be in parallel with that of the internal corner points, the height of an α-form particle is computed as

$$S_{\mathrm{h}} = \frac{1}{4}\sum_{n=1}^{8} {d_{\mathrm{h}}}^n \tag{28}$$

where ${d_{\mathrm{h}}}^n$, $n = 1, 2, \cdots, 8$ denotes the distances between the point P_{e}^n and the fitting plane of $(P_{\mathrm{i}}^1, P_{\mathrm{i}}^2, P_{\mathrm{i}}^3, P_{\mathrm{i}}^4)$, the point P_{i}^n and the fitting plane $(P_{\mathrm{e}}^1, P_{\mathrm{e}}^2, P_{\mathrm{e}}^3, P_{\mathrm{e}}^4)$, respectively. Note that owing to the α-form particle is symmetrical with respect to the fitting plane composed of the external corner points, the height is computed as double of the averaged distance between these two fitting planes.

For a β-form particle, the identified key corners are used to reconstruct a 3D geometry model of the cuboid shape. Owing to that the cuboid shape could be efficiently approximated by the minimum-volume bounding box approach [40, 41], 3D sizes of a β-form particle can therefore be measured by using this approach for the reconstructed cuboid.

Based on the above measured 3D sizes, the particle volume can be quantitatively computed, such as from a reconstructed cuboid. However, such computation may give rise to undesirable estimation error. To improve the computation accuracy, it is proposed to view the reconstructed particle shape as a convex hull for computation. By using the Delaunay triangulation principle [42], a convex hull can be subdivided into N_s tetrahedrons. Denote by $\{(x_{t,n}, y_{t,n}, z_{t,n}), t = 1,...,4, n = 1,...,N_s\}$ four vertex coordinates of the n-th tetrahedron, the volume of the n-th tetrahedron can be computed as

$$V_n = \frac{1}{6} \times \begin{vmatrix} 1 & 1 & 1 & 1 \\ x_{1,n} & x_{2,n} & x_{3,n} & x_{4,n} \\ y_{1,n} & y_{2,n} & y_{3,n} & y_{4,n} \\ z_{1,n} & z_{2,n} & z_{3,n} & z_{4,n} \end{vmatrix} \tag{29}$$

Accordingly, the particle volume is estimated based on the symmetry as

$$V = 2\sum_{n=1}^{N_s} V_n \tag{30}$$

5. Experimental results

Two cooling crystallization experiments on α- and β-form LGA were performed, respectively, based on the non-invasive binocular imaging system for 3D morphology measurement, with the same experimental conditions introduced in Section 2, except for the cooling rates of 1°C/min for α-form LGA and 0.2°C/min for β-form LGA. Note that to transform the image pixel into a physical unit for computation, the calibration method [11] with circle scale was used to obtain the pixel equivalent before the measurement. For comparison, an off-line electron microscope (Leica DM 2500, LAS_v4.4) was also used for verifying the sizes and volumes of final crystal products.

Before 3D reconstruction of particle shapes, image processing was conducted for in-situ captured double-view images of α-form LGA crystals during the crystallization process, as shown in Fig.6. For illustration, a pair of the original double-view images including α-form crystals is

shown in Fig.6a. Fig.6b shows the preprocessed image pair of the outlined α-form crystal in Fig.6a by the Canny method. Using the proposed corner detection method for α-form crystals, Fig.6c shows the detected results of external and internal contour edges of this α-form crystal. Accordingly, the corner detection results are shown in Fig.6d, well demonstrating that the proposed image analysis method effectively detected the key corners in real time. The detected key corners were then used for 3D reconstruction of this crystal shape.

A reconstructed stereo shape of α-form crystals is illustrated in Fig.7. The 3D coordinates of the eight key corners are computed by the proposed geometry model formulae, as shown in Fig.7a. The correspondingly reconstructed 3D geometry model is shown in Fig.7b. Note that the symmetry of an α-form crystal should be considered in the final geometry reconstruction, which is omitted.

Similarly, a stereo reconstruction of β-form LGA crystals is illustrated in Fig.8, based on the in-situ captured double-view images. Fig.8a shows the in-situ captured images of β-form crystals. After image preprocessing, the segmented double-view images for a sampled β-form crystal are shown in Fig.8b. Then Fig.8c shows the corner detection results for this β-form crystal. Finally, a stereo shape of this β-form crystal is approximately reconstructed based on the corresponding key corners, as shown in Fig.8d.

Note that the total time spent for the proposed method to measure the 3D sizes of an α- form LGA crystal was about 1.52 seconds, and about 1.48 seconds for a β-form LGA crystal, based on a monitoring computer configured with CPU of Intel 3.40 GHZ and RAM of 8.00G. The time was sufficiently small for implementing an on-line control strategy as studied in the recent paper [43], where the sampling time for control implementation was taken as tens of second or even a few minutes for LGA cooling crystallization.

To demonstrate the effectiveness of the proposed method, an off-line measurement of CSD using an electron microscope was also performed on the final crystal products for verification. In view of that an electron microscope could only measure the 2D sizes of each crystal, comparison between the proposed method and an electron microscope was therefore made for measuring the CSDs in length and width for LGA crystal products of α-and β-forms, respectively. Almost 200 particles randomly taken from the LGA crystal products were used for measuring CSD of α- and

β-form crystals, respectively. For illustration, the measured CSDs were fitted by the probability density estimation with the normal kernel function [44]. The measured CSD results are plotted in Fig.9 in comparison with off-line measurement by an electron microscope based on the pre-processed samples of LGA crystal products, well demonstrating the consistency between each other.

To further demonstrate the superiority of the proposed method over the recently developed 2D size measurement method [11] based on the image projection of a particle in a 2D fitting plane, Table 2 shows a comparison of relative errors between the proposed method (denoted by 3DM) and the 2D size measurement method (denoted by 2DM) with reference to the off-line measurement by an electron microscope, where the peak size denotes the peak value of CSD. It is seen that evidently improved accuracy on the 2D size measurement is obtained by the proposed method.

In view of that the above LGA crystal products are too tiny in volume to be measured by an electron microscope for off-line verification, the needle-like monosodium glutamate crystals with relatively larger 3D sizes of millimeter-scale were used to verify the proposed volume computation method, owing to that their shapes are similar to β-form LGA crystals and these particles can be manually deployed for in-situ or off-line measurement. The experiment was carried out by fixing thee needle-like monosodium glutamate crystals on the inside wall of the glass crystallizer for in-situ measurement by the non-invasive binocular imaging system, as shown in Fig.10(a). The proposed volume computation method is therefore used based on 3D shape reconstruction. For comparison, the off-line measurement was conducted by measuring two side faces (length×width and length×height) of each particle with an off-line electron microscope for computing the particle volume, as shown in Fig.10(b). The measurement results are listed in Table 3. It is seen that the in-situ measurement results by the proposed method are in good agreement with the off-line measurement by an electron microscope, with averaged relative errors below 10%. These results well demonstrates that the proposed method can be effectively used for in-situ assessment of particle volumes during the crystallization process, thus facilitating on-line monitoring of crystal growth kinetics and quality.

6. Conclusions

An in-situ measurement method has been proposed for monitoring 3D CSD during a crystallization process, based on double-view images simultaneously captured by a non-invasive binocular micro-vision system. By detecting the particle edges from the captured double-view images with fast image preprocessing algorithms to overcome the influence from solution turbulence and uneven illumination background involved with in-situ imaging, two fast algorithms for real-time implementation are proposed to locate the key corners in the captured images for two typical crystal morphologies of prismatic and needle-like shapes, such as α- and β-forms of LGA, respectively. Based on the identified key corners, a 3D geometry model is established to approximate the 3D shape of each captured particle. Two fast algorithms are given to compute 3D sizes of α- and β-form LGA crystals from the reconstructed 3D shapes, respectively. In addition, a tetrahedron based fast algorithm is given to quantitatively measure the volume of each imaged particle. Experimental tests on the cooling crystallization processes of α- and β-form LGA crystals have well demonstrated the effectiveness of the proposed method for in-situ monitoring 3D crystal morphologies, with good accuracy on measuring the length and width of crystals in comparison with off-line measurement by an electron microscope or the recent 2D crystal size measurement method given in the previous work [11]. Moreover, the in-situ measurement accuracy on particle volume by the proposed method is validated via needle-like monosodium glutamate crystals, in comparison with off-line measurement by an electron microscope. It should be noted that the accuracy of such a 3D geometry model for approximation depends on the identified key corners. If no sufficient key corners could be detected for a particle image, its 3D morphology may not be completely reconstructed, in particular for very small particles that could not be effectively imaged. It therefore deserves a further study on multi-directional imaging with more cameras or a predefined data set to facilitate 3D shape reconstruction in the future work, along with real-time classification methods on different particle shapes.

Acknowledgements

This work was supported in part by the NSF China Grant 61633006, the Fundamental Research Funds for the Central Universities of China (DUT18ZD201), and National Key RD Program of China under Grant 2017YFA0700300.

References

(1) Yu, Z.; Chew, J.; Chow, P.; Tan, R., Recent advances in crystallization control: an industrial perspective. *Chemical Engineering Research and Design* **2007,** 85, (7), 893-905.
(2) Wang, X. Z.; Roberts, K. J.; Ma, C., Crystal growth measurement using 2D and 3D imaging and the perspectives for shape control. *Chemical Engineering Science* **2008,** 63, (5), 1173-1184.
(3) Nagy, Z. K.; Fevotte, G.; Kramer, H.; Simon, L. L., Recent advances in the monitoring, modelling and control of crystallization systems. *Chemical Engineering Research and Design* **2013,** 91, (10), 1903-1922.
(4) Borsos, A. k.; Szilagyi, B.; Agachi, P. S. e.; Nagy, Z. K., Real-time image processing based online feedback control system for cooling batch crystallization. *Organic Process Research & Development* **2017,** 21, 511-519.
(5) Anda, J. C. D.; Wang, X. Z.; Lai, X.; Roberts, K. J.; Jennings, K. H.; Wilkinson, M. J.; Watson, D.; Roberts, D., Real-time product morphology monitoring in crystallization using imaging technique. *AIChE Journal* **2005,** 51, (5), 1406-1414.
(6) Ferreira, A.; Faria, N.; Rocha, F.; Teixeira, J., Using an online image analysis technique to characterize sucrose crystal morphology during a crystallization run. *Industrial & Engineering Chemistry Research* **2011,** 50, (11), 6990-7002.
(7) Hansen, T. B.; Simone, E.; Nagy, Z.; Qu, H., Process analytical tools to control polymorphism and particle size in batch crystallization processes. *Organic Process Research & Development* **2017,** 21, 855-865.
(8) Gao, Z.; Wu, Y.; Bao, Y.; Gong, J.; Wang, J.; Rohani, S., Image analysis for in-line measurement of multidimensional size, shape, and polymorphic transformation of L-glutamic acid using deep learning-based image segmentation and classification. *Crystal Growth & Design* **2018,** 18, (8), 4275-4281.
(9) Eisenschmidt, H.; Voigt, A.; Sundmacher, K., Face-Specific growth and dissolution kinetics of potassium dihydrogen phosphate crystals from batch crystallization experiments. *Crystal Growth & Design* **2015,** 15, (1), 219-227.
(10) Liao, C. W.; Yu, J. H.; Tarng, Y. S., On-line full scan inspection of particle size and shape using digital image processing. *Particuology* **2010,** 08, (3), 286-292.
(11) Huo, Y.; Liu, T.; Liu, H.; Ma, C. Y.; Wang, X. Z., In-situ crystal morphology identification using imaging analysis with application to the L-glutamic acid crystallization. *Chemical Engineering Science* **2016,** 148, 126-139.
(12) Zhou, Y.; Srinivasan, R.; Lakshminarayanan, S., Critical evaluation of image processing approaches for real-time crystal size measurements. *Computers & Chemical Engineering* **2009,** 33, (5), 1022-1035.
(13) Arnaout, T. E.; Cullen, P. J.; Sullivan, C., A novel backlight fiber optical probe and image algorithms for real time size-shape analysis during crystallization. *Chemical Engineering Science* **2016,** 149, 42-50.
(14) Zhang, R.; Ma, C. Y.; Liu, J. J.; Wang, X. Z., On-line measurement of the real size and shape of crystals in stirred tank crystalliser using non-invasive stereo vision imaging. *Chemical Engineering Science* **2015,** 137, (10), 9-21.
(15) Larsen, P.; Rawlings, J.; Ferrier, N., Model-based object recognition to measure crystal size and shape distributions from in situ video images. *Chemical Engineering Science* **2007,** 62, (5), 1430-1441.
(16) Larsen, P.; Rawlings, J.; Ferrier, N., An algorithm for analyzing noisy, in situ images of high-aspect-ratio crystals to monitor particle size distribution. *Chemical Engineering Science* **2006,** 61, (16), 5236-5248.
(17) Zhang, Y.; Zhang, J.; Jorge, C. A.; Wang, X. Z., Particle shape characterisation and classification using automated microscopy and shape descriptors in batch manufacture of particulate solids. *Particuology* **2016,** 24, (1), 61-68.
(18) Schorsch, S.; Vetter, T.; Mazzotti, M., Measuring multidimensional particle size distributions during crystallization. *Chemical Engineering Science* **2012,** 77, (1), 130-142.
(19) Ma, C. Y.; Liu, J. J.; Wang, X. Z., Measurement, modelling, and closed-loop control of crystal shape distribution: Literature review and future perspectives. *Particuology* **2016,** 26, (3), 1-18.
(20) Zhang, R.; Ma, C. Y.; Liu, J. J.; Zhang, Y.; Liu, Y. J.; Wang, X. Z., Stereo imaging camera model for 3D shape reconstruction of complex crystals and estimation of facet growth kinetics. *Chemical Engineering Science* **2017,** 160, 171-182.
(21) Bujak, B.; Bottlinger, M., Three-dimensional measurement of particle shape. *Particle & Particle Systems Characterization* **2008,** 25, (4), 293-297.
(22) Chakraborty, J.; Sarkar, D.; Singh, A.; Bharti, A. K., Measuring the three-dimensional morphology of crystals using regular reflection of light. *Crystal Growth & Design* **2012,** 12, (12), 6042-6049.
(23) Kempkes, M.; Vetter, T.; Mazzotti, M., Measurement of 3D particle size distributions by stereoscopic imaging. *Chemical Engineering Science* **2010,** 65, (4), 1362-1373.
(24) Schorsch, S.; Ochsenbein, D. R.; Vetter, T.; Morari, M.; Mazzotti, M., High accuracy online measurement of multidimensional particle size distributions during crystallization. *Chemical Engineering Science* **2014,** 105, 155-168.
(25) Borchert, C.; Temmel, E.; Eisenschmidt, H.; Lorenz, H.; Seidel-morgenstern, A.; Sundmacher, K., Image-based in situ identification of face specific crystal growth rates from crystal populations. *Crystal Growth & Design* **2014,** 14, (3), 952–971.
(26) Rajagopalan, A. K.; Schneeberger, J.; Salvatori, F.; Bötschi, S.; Ochsenbein, D. R.; Oswald, M. R.; Pollefeys, M.; Mazzotti, M., A comprehensive shape analysis pipeline for stereoscopic measurements of particulate populations in suspension. *Powder Technology* **2017,** 321, 479-493.

(27) Ma, C. Y.; Liu, J. J.; Wang, X. Z., Stereo imaging of crystal growth. *AIChE Journal* **2016,** 62, (1), 18-25.
(28) Wu, K.; Ma, C. Y.; Liu, J. J.; Zhang, Y.; Wang, X. Z., Measurement of crystal face specific growth kinetics. *Crystal Growth & Design* **2016,** 16, (9), 4855-4868.
(29) Chen, Z.; Liao, H.; Zhang, X., Telecentric stereo micro-vision system: calibration method and experiments. *Optics & Lasers in Engineering* **2014,** 57, 82-92.
(30) Schreier, H. W.; Garcia, D.; Sutton, M. A., Advances in light microscope stereo vision. *Experimental Mechanics* **2004,** 44, (3), 278-288.
(31) Huo, Y.; Liu, T.; Wang, X. Z.; Ma, C. Y.; Ni, X., Online detection of particle agglomeration during solution crystallization by microscopic double-view image analysis. *Industrial & Engineering Chemistry Research* **2017,** 56, 11257-11269.
(32) And, E. S. F.; Davey, R. J., Solution-mediated transformation of α to β l-glutamic acid: rate enhancement due to secondary nucleation. *Crystal Growth & Design* **2004,** 4, (5), 1061–1068.
(33) Gonzales, R. C.; Woods, R. E.; Eddins, S. L., *Digital image processing using MATLAB*. Pearson Prentice Hall: Upper Saddle River, NJ, 2004.
(34) Calderon De Anda, J.; Wang, X. Z.; Roberts, K. J., Multi-scale segmentation image analysis for the in-process monitoring of particle shape with batch crystallisers. *Chemical Engineering Science* **2005,** 60, (4), 1053-1065.
(35) Calderon De Anda, J.; Wang, X. Z.; Lai, X.; Roberts, K. J., Classifying organic crystals via in-process image analysis and the use of monitoring charts to follow polymorphic and morphological changes. *Journal of Process Control* **2005,** 15, (7), 785-797.
(36) Mokhtarian, F.; Suomela, R., Robust image corner detection through curvature scale space. *IEEE Transactions on Pattern Analysis & Machine Intelligence* **1998,** 20, (12), 1376-1381.
(37) Awrangjeb, M.; Lu, G., An improved curvature scale-space corner detector and a robust corner matching approach for transformed image identification. *IEEE Transactions on Image Processing* **2008,** 17, (12), 2425-2441.
(38) Calonder, M.; Lepetit, V.; Strecha, C.; Fua, P. In *BRIEF: binary robust independent elementary features*, European Conference on Computer Vision, Heraklion, 2010; Springer: Heraklion, 2010; pp 778-792.
(39) Acharya, P. K.; Henderson, T. C. In *Parameter estimation and error analysis of range data*, 1988 IEEE International Conference on Robotics and Automation, Philadelphia, 1988; Philadelphia, 1988; pp 1709-1714.
(40) Barequet, G.; Har-Peled, S., Efficiently approximating the minimum-volume bounding box of a point set in three dimensions. *Journal of Algorithms* **2001,** 38, (1), 91-109.
(41) Barber, C. B.; Dobkin, D. P.; Huhdanpaa, H., The quickhull algorithm for convex hulls. *ACM Transactions on Mathematical Software* **1996,** 22, (4), 469-483.
(42) Fang, T. P.; Piegl, L. A., Delaunay triangulation in three dimensions. *Computer Graphics & Applications IEEE* **1995,** 15, (5), 62-69.
(43) Zhang, F.; Liu, T.; Huo, Y.; Guan, R.; Wang, X. Z., Investigation of the operating conditions to morphology evolution of β-l-glutamic acid during seeded cooling crystallization. *Journal of Crystal Growth* **2017,** 469, 136–143.
(44) Bowman, A. W.; Azzalini, A., *Applied smoothing techniques for data analysis*. Oxford University Press: New York, 1997.

Appendix: Derivation of Eq.(10)

From Fig.4a, the following two equations stand according to the common property of two similar triangles,

$$\frac{Z-f_c}{Z}=\frac{b_1-a_1}{b_1} \tag{A1}$$

$$\frac{Z-f_c}{Z}=\frac{b_2-a_2}{b_2} \tag{A2}$$

where $f_c=f\cos\theta$ and $b_1+b_2=b$.

The above equations can be equivalently transformed into

$$\frac{b_1-a_1}{Z-f_c}=\frac{b_1}{Z} \tag{A3}$$

$$\frac{b_2-a_2}{Z-f_c}=\frac{b_2}{Z} \tag{A4}$$

Since $b_1+b_2=b$, it can be derived that

$$Z=\frac{bf_c}{a_1+a_2} \tag{A5}$$

Fig.4b shows the geometric diagram in the left view of camera. According to the sine law, there follows

$$\frac{\sin(90+\tau_l)}{m_l}=\frac{\sin(90-\theta-\tau_l)}{x_l} \tag{A6}$$

where $n_l=f\sin\theta$.

It can be derived from (A6) that

$$m_l=\frac{x_l\sin(90+\tau_l)}{\sin(90-\theta-\tau_l)} \tag{A7}$$

It can be seen from Fig.4b that

$$a_1=m_l+n_l \tag{A8}$$

Since Fig.4c shows the geometric diagram in the right view of camera, it follows from the sine law that

$$\frac{\sin(90-\tau_r)}{m_r}=\frac{\sin(90-\theta+\tau_r)}{x_r} \tag{A9}$$

where $n_r=f\sin\theta-m_r$.

It can be derived from (A9) that

$$m_r=\frac{x_r\sin(90-\tau_r)}{\sin(90-\theta-\tau_r)} \tag{A10}$$

It can be seen from Fig.4c that

$$a_2 = n_r \tag{A11}$$

Therefore,

$$a_1 + a_2 = m_l + n_l + n_r \tag{A12}$$

By substituting (A12) into (A5), it yields

$$Z = \frac{bf\cos\theta}{2f\sin\theta + \dfrac{x_l \sin(90+\tau_l)}{\sin(90-\theta-\tau_l)} + \dfrac{x_r \sin(90-\tau_r)}{\sin(90-\theta+\tau_r)}} \tag{A13}$$

which may be rewritten as

$$Z = \frac{bf\cos\theta}{2f\sin\theta + \dfrac{x_l \cos\tau_l}{\cos(\theta+\tau_l)} - \dfrac{x_r \cos\tau_r}{\cos(\theta-\tau_r)}} \tag{A14}$$

where $\tan\tau_l = x_l / f$, $x_l = \dfrac{\gamma}{\kappa}\left|u_l - L/2\right|$, $\tan\tau_r = x_r / f$, and $x_r = \dfrac{\gamma}{\kappa}\left|u_r - L/2\right|$.

List of Table and Figure Captions

Table 1 Measurement errors on a micro-scale rule with a dip angle of 65°

True length (μm)	500 (B-C)	1000 (A-C)	1500 (A-D)	Averaged relative error (%)
Measured length (μm)	481.18	976.32	1427.83	3.65
Measured dip angle (°)	60.35	61.92	63.28	4.85

Table 2 Comparison of relative measurement errors (%) between the proposed method and a 2D measurement method with reference to offline measurement by an electron microscope

Method	Size	α-form		β-form		Averaged relative error (%)
		Length (μm)	Width (μm)	Length (μm)	Width (μm)	
3DM	Mean	3.28	2.87	4.16	3.73	3.58
	Peak	4.39	3.29	3.08	3.84	
2DM	Mean	7.97	7.48	7.92	4.78	7.19
	Peak	8.25	6.71	8.74	5.63	

Table 3 Volume measurement errors on three different monosodium glutamate particles

Item	Particle 1	Particle 2	Particle 3
Off-line verification (mm^3)	0.462	0.371	0.355
The proposed method (mm^3)	0.419	0.338	0.323
Relative error (%)	9.31	8.89	9.01

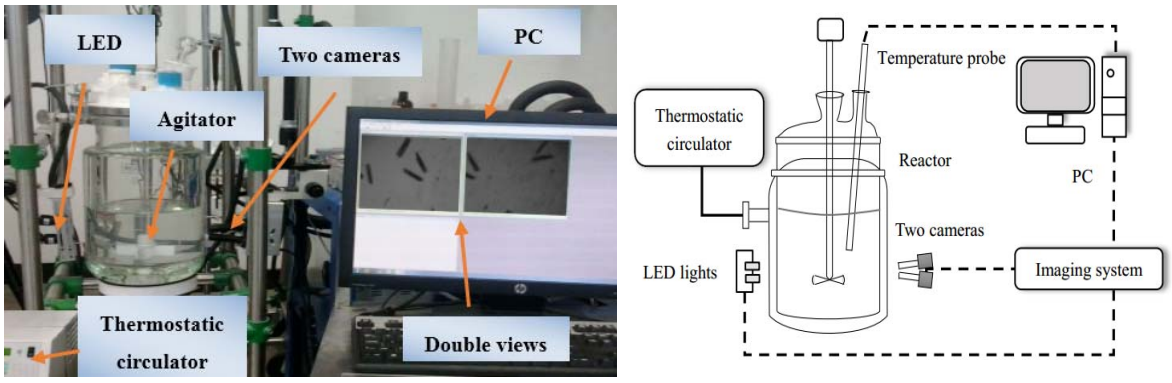

(a) (b)

Fig.1 Non-invasive binocular micro-vision system for monitoring a crystallization process: (a) external view; (b) schematic diagram.

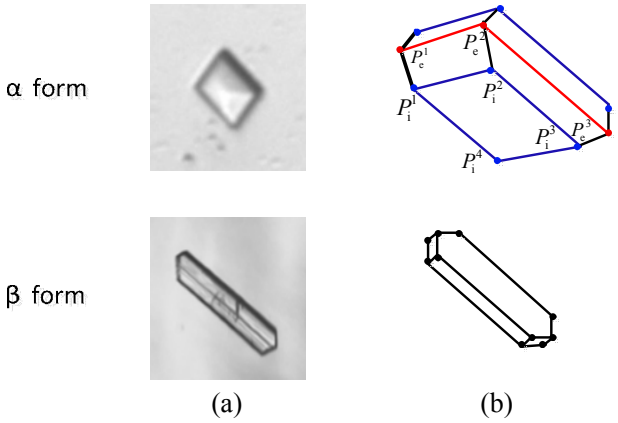

Fig.2 LGA crystal morphologies of α- and β-forms: (a) crystal images; (b) simplified reconstructions (external contour edges are marked in red and internal contour edges are marked in blue for α form).

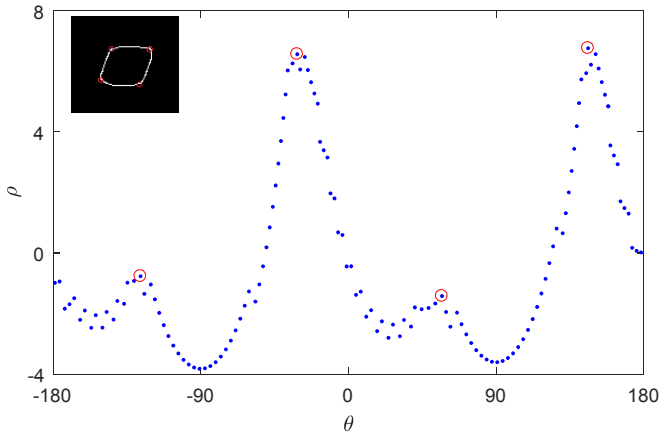

Fig.3 Plot of the inner distances of contour points in an α-form crystal image (The contour image is in the top left corner and the extremum points are marked in red).

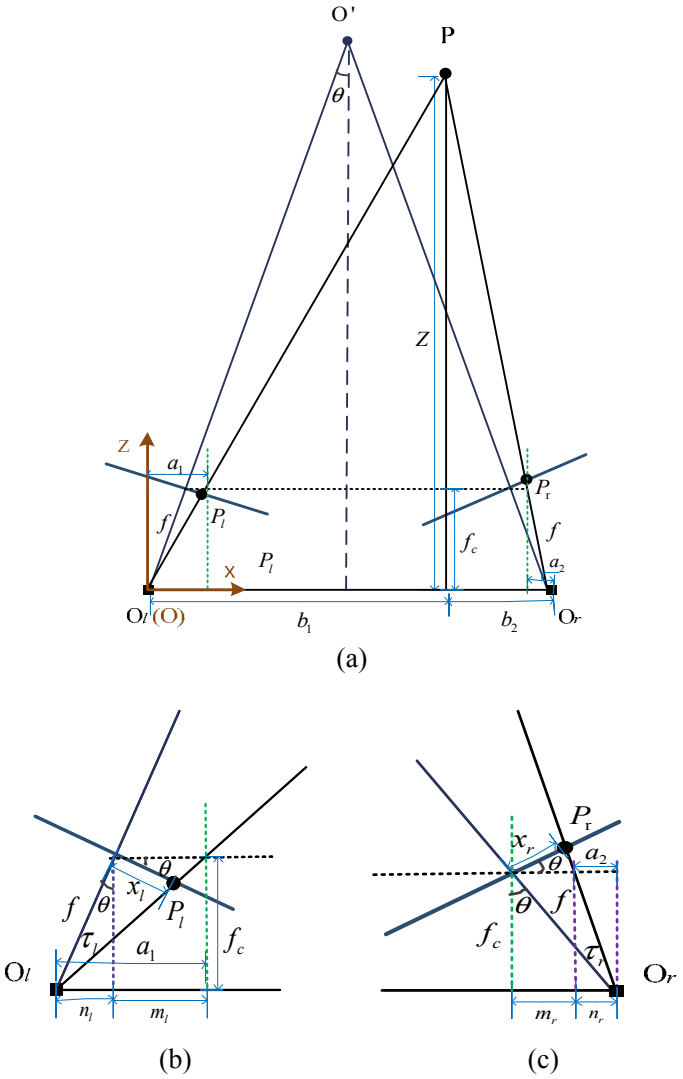

Fig.4 The geometry model of a stereo imaging system: (a) stereo imaging; (b) the left-view model; (c) the right-view model.

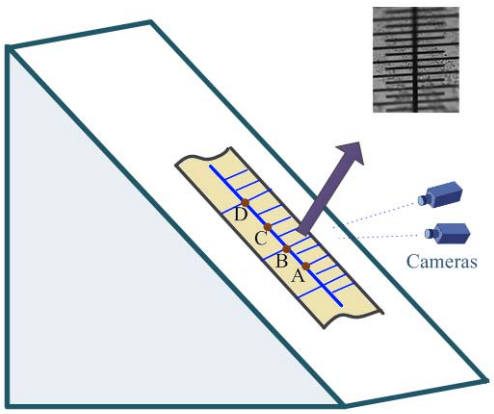

Fig.5 Schematic diagram of the measurement test on a micro-scale ruler.

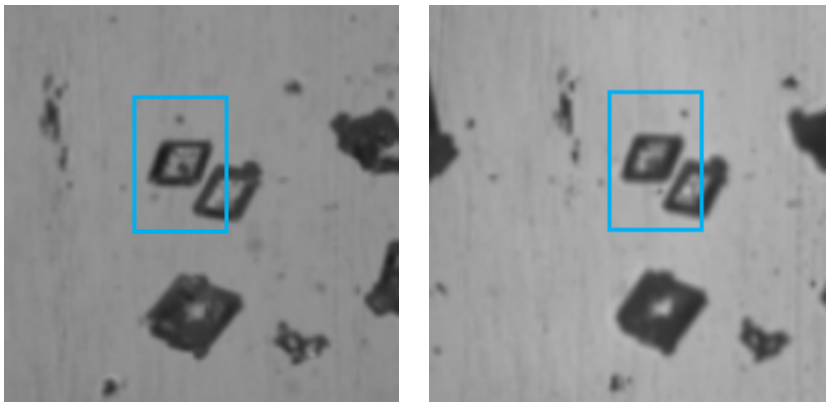

(a)

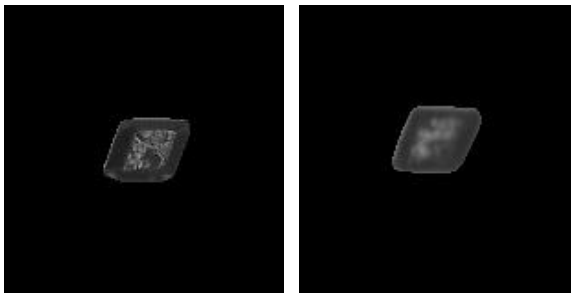

(b)

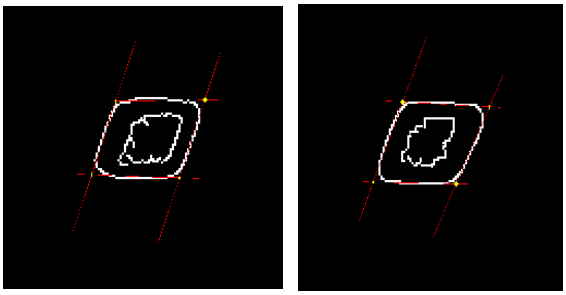

(c)

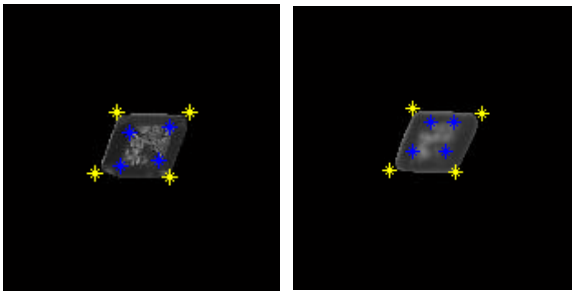

(d)

Fig.6 Image processing results for α-form LGA crystals: (a) original double-view images; (b) segmented double-view images for a sampled crystal; (c) external and internal contours; (d) the key corners.

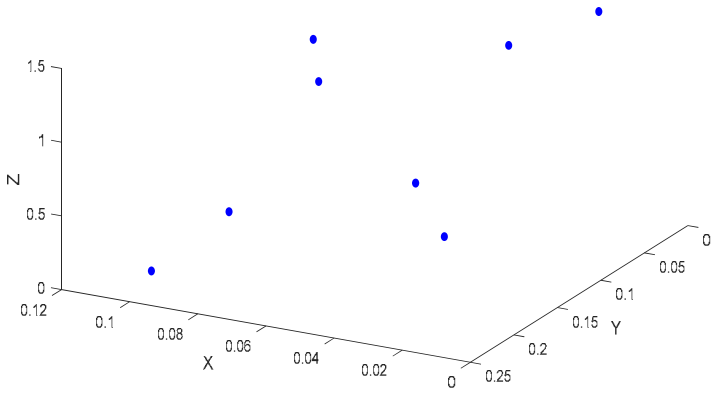

(a)

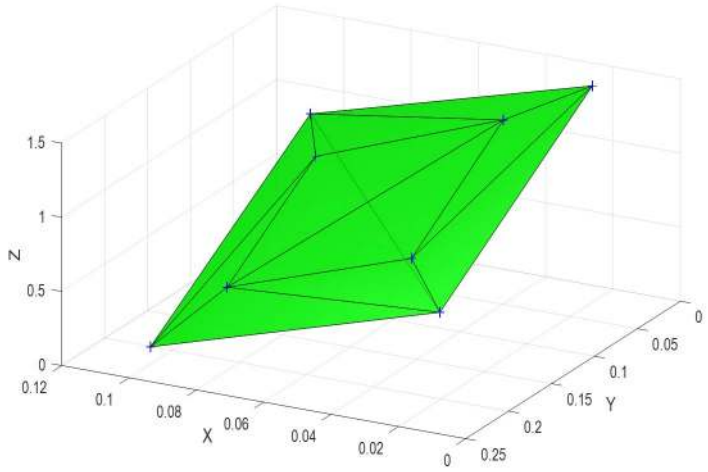

(b)

Fig.7 3D shape reconstruction for an α-form LGA crystal: (a) 3D locations of the key corners; (b) 3D shape reconstruction.

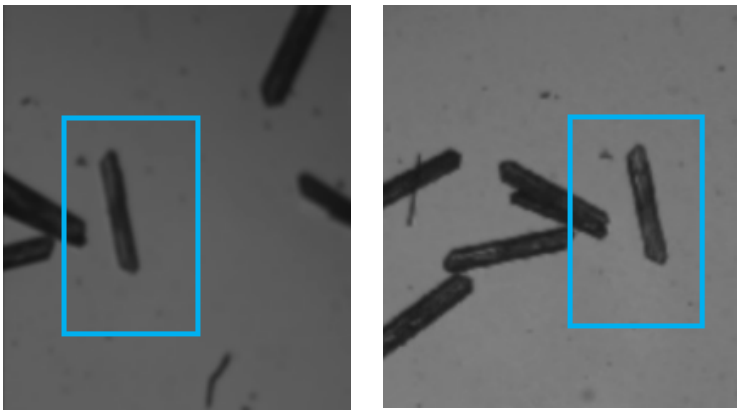

(a)

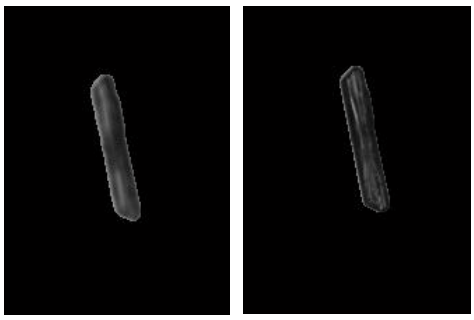

(b)

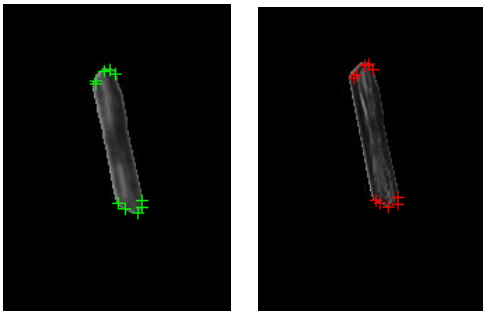

(c)

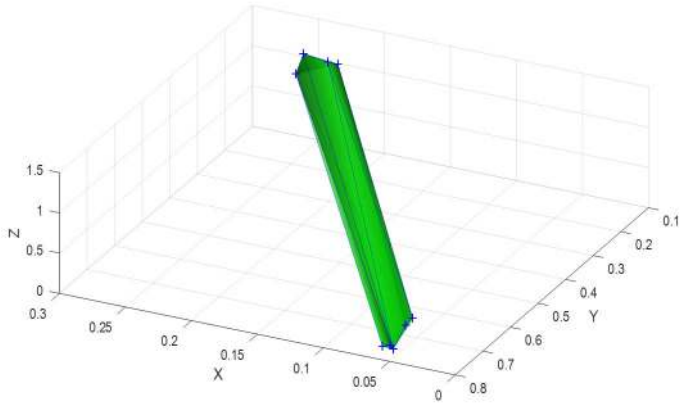

(d)

Fig.8 Illustration of image processing and 3D reconstruction results for a β-form LGA crystal: (a) original double-view images; (b) segmented double-view images for a sampled crystal; (c) key corner detection; (d) 3D shape reconstruction.

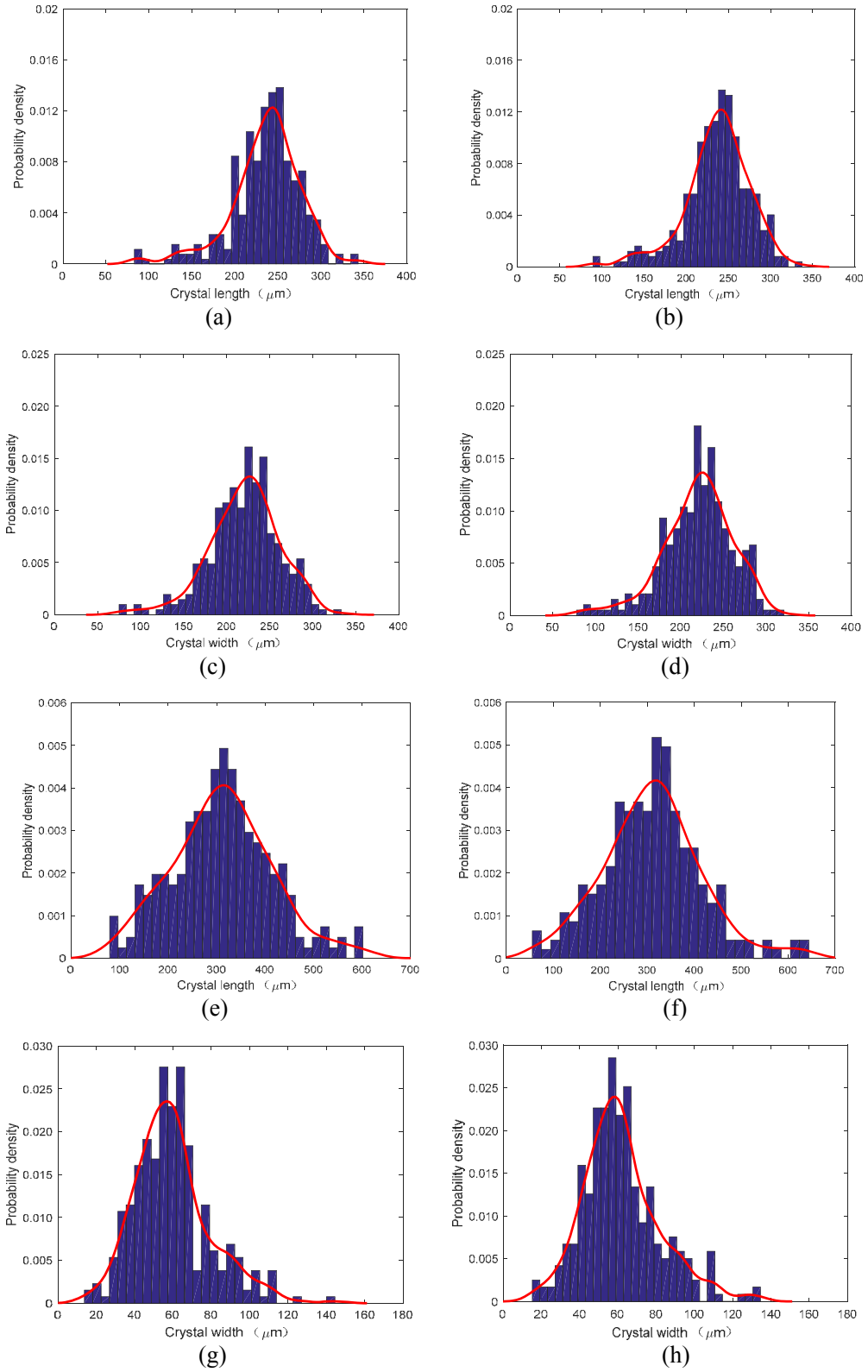

Fig.9 In-situ measured results of LGA CSD compared to off-line measurement by an electron microscope: (a) the length distribution of α-form LGA by the proposed method; (b) the length distribution of α-form LGA by off-line measurement of microscopy; (c) the width distribution of α-form LGA by the proposed method; (d) the width distribution of α-form LGA by off-line measurement of microscopy; (e) the length distribution of β-form LGA by the proposed method; (f) the length distribution of β-form LGA by off-line measurement of microscopy; (g) the width distribution of β-form LGA by the proposed method; (h) the width distribution of β-form LGA by off-line measurement of microscopy.

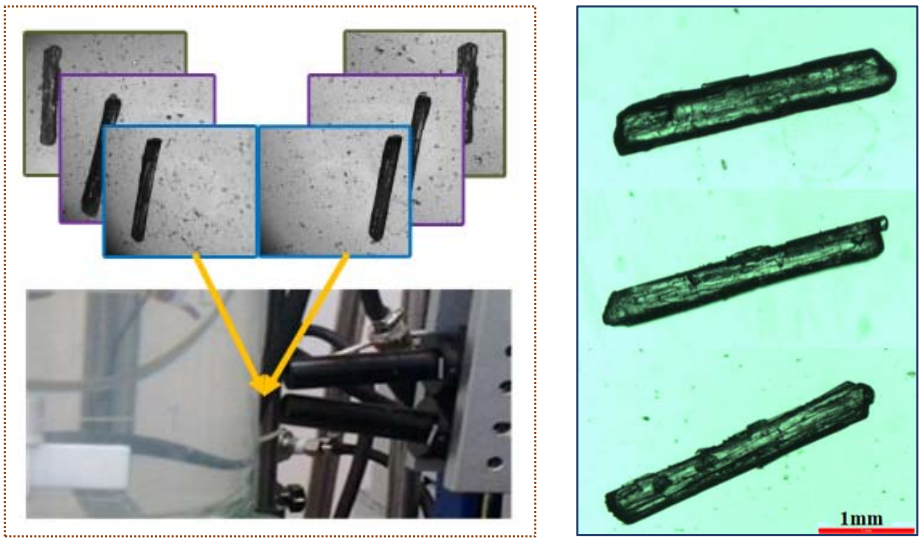

(a) (b)

Fig.10 Experimental verification on volume computation via monosodium glutamate particles: (a) the proposed method based on in-situ double-view imaging; (b) off-line measurement on three different monosodium glutamate crystals by an electron microscope.